Photodissociation and Photoionization Dynamics in the Extreme Ultraviolet Region Studied by Synchrotron Radiation-Laser Combination Techniques

Hiromichi Niikura

Doctor of Philosophy

Department of Structural Molecular Science,
School of Mathematical and Physical Science,
The Graduate University for Advanced Studies

1999

Acknowledgments

I would like to express the gratitude to Prof. Dr. Koichiro Mitsuke, associate professor of IMS, for his guidance and discussions. Special thank is due to the members of the UVSOR facility, Laser Research Center and Laboratory of Chemical Dynamics in IMS for their help during the course of the experiments. I would like to thank Prof. Dr. Satoshi Hirayama of Kyoto Institute of Technology for scientific education. I express appreciation for the financial support from Japan Society for the Promotion of Science (J.S.P.S.). This work was partly supported by Grant-in-Aids (Nos. 10640504 and 199808226) for Scientific Research from the Ministry of Education, Science, Sports and Culture, Japan. Finally, I am grateful to my parents, Yoshiko and Takeshi Niikura.

January 2000

Hiromichi Niikura

Chapter 1
General Introduction

Development of a new experimental setup has always stimulated the progress in the theoretical and experimental attempts on molecular sciences. Last two or three decades, lasers and synchrotron radiation have been powerful tools for investigating the molecular structure and their dynamical features as excitation and/or probing light sources. Synchrotron radiation has enabled us to utilize the wide photon energy ranging from infrared to hard X ray continuously [1], while various type of lasers with the high photon flux and excellent temporal or spectral resolutions have brought us the information on the detailed structures of molecules and the ultrashort dynamical phenomena in the photon energy of infrared (IR), visible (VIS) and ultraviolet (UV) region [2]. Applying these two kinds of light sources simultaneously, new kind of pump-probe or double resonance spectroscopy will be developed for investigating phenomena occurred in the wide photon energy range in a more detailed manner.

Combination experiments of laser and synchrotron radiation have been preliminary performed in a few synchrotron radiation facilities. *Mitani et al.* have synchronized successive pulses of synchrotron radiation from UVSOR (Okazaki, Japan) with the picosecond light pulse of a cw mode-locked Nd: YAG laser, and measured the transient absorption spectra of the electronic excited singlet state of Rodamine 6 G in solution in a short time domain of 0.05 - 11 ns [3]. The lifetimes of excited atoms such as $Xe^*(5p^5 5d)$, $He^*(1s3p)$ and Ca^* have been measured with a time-resolved pump-probe photoelectron spectroscopy by synchronizing the pulses of the mode-locked laser and synchrotron radiation [4-5]. The perfect synchronization of the 90.115 MHz pulses of undulator radiation with the mode-locked Ti:sapphire laser has been recently performed in UVSOR [6] and confirmed lifetime of $He^*(1s2p)$ of ~ 500 ps. Combination experiments has also been applied to the gas phase molecular dynamics, but experimental examples have been limited [6,7-8]. *Nahon et al.* have dissociated *s*-tetrazine by photoexcitation with a cw visible laser and probed the vibrational state distribution of

fragments by synchrotron radiation ionization with photoelectron spectroscopy [7].

In this study, synchrotron radiation and laser combination experiments are applied for the study of the molecular photoionization and photodissociation dynamics observed in extreme ultraviolet (2 - 1000 Å , XUV) region [9]. In contrast to the previous laser-synchrotron radiation combination experiments, molecules are dissociated and/or ionized by synchrotron radiation photoexcitation, and their photoproducts are detected by laser spectroscopy. Using synchrotron radiation as an excitation source, we can excite the molecules at the photon energy which is rather difficult to be accessed by laser excitation[#1]. In addition, lasers with a good spectral resolution are found to be very useful for probing the internal state of photoproducts as described in detail later in this section.

Molecular superexcited states, located in the XUV region, provide interesting physical systems in which the excited electrons interact with both the molecular ion core and the other electrons, leading to the various type of autoionization and/or predissociation [11]. They are also recognized as the quasi-bound state interacting with the two different types of the open channels. Superexcited state is defined as the neutral excited state whose internal energy is larger than that of the lowest ionization limit, and are classified into Rydberg and valence types [11]. The former has the electronic configuration including the excitation into a Rydberg orbital, and the latter into a valence orbitals. Excitation and decay processes including superexcited states, ABC^{**}, are summarized as follows :

$ABC \xrightarrow{h\nu}$	$ABC^+ + e^-$	Direct Ionization	(1)
$\hookrightarrow ABC^{**} \rightarrow$	$ABC^+ + e^-$	Autoionization	(2)
	$\rightarrow AB + C$	Neutral Dissociation	(3)
	$\rightarrow AB^+ + C^-$	Ion Pair Formation	(4)

Direct ionization is usually associated with the excitation of superexcited states due to the contribution of the oscillator strength from the electronically ground states to the ionization

---

[#1] Recently, development in ultrafast laser techniques enables us to generate the XUV and X-ray pulses with femto or atto second time resolution [10].

continua directly. Fragmentation, photoemission, and fragment autoionization processes succeed when the ions and neutral fragments are (super) excited :

$$ABC^{*+} \rightarrow AB + C^{+} \qquad \text{Fragmentation} \qquad (5)$$

$$\rightarrow ABC^{+} + h\nu \qquad \text{Emission} \qquad (6)$$

$$AB^{**} \rightarrow AB + e^{-} \qquad \text{Fragment autoionization} \qquad (7)$$

Here, AB^{**} represent the superexcited states and ABC^{*+} represents the electronically excited ions. In this thesis, the photoproducts are divided into three categories, *ions*, *fragment ions* and *neutral fragments*. Ions represents those produced by autoionization or direct ionization process, fragment ions are from the process of (5), and neutral fragments are from the process (3). The positive fragment ion have been also observed as the photoproducts of (4), but the yield of this process is quite low [12].

Autoionization process are classfied into two types according to the way of interaction between the superexcited states and ionization continua: One is the *vibronal* or *rotational* autoionization process induced by the coupling between nuclear *translational* or *rotational* motion and electronic motion, respectively, and is recognized as the non-adiabatic transition process [11]. Vibrational (rotational) autoionization proceeds in the Rydberg states whose vibrational (rotational) energy is larger that the ionization limit, keeping the same electronic configuration except the out going Rydberg electron. The other is *electronic* autoionization induced by the configuration interaction between Rydberg states and ionization continua. Electronic autoionization proceeds in the Rydberg states converging to the ionization limit of the electronically excited states of ion, rearranging the electronic configuration involving more than two electrons. The neutral dissociation proceeds through the optical transition to the Rydberg states interacting with the valence superexcited states, the way of interaction has been treated as the electronic coupling between Rydberg and valence states [13]. Actually, these two kinds of interactions, electron-nuclei interactions and configuration interaction of electron, would be involved in any type of autoionization and/or dissociation processes, so it is the central interest to clarify experimentally what kind of interactions plays an important role for each decay process.

Rydberg superexcited states have been observed in the absorption, ionization spectra, positive fragment ion yield curves, constant-ionic-state photoelectron spectra, and threshold photoelectron spectra of small diatomic and polyatomic molecules [14-15]. They sometimes show the asymmetric line structures called Fano Profiles [16]. These line shapes and quantum defects reflect the interaction of Rydberg states with the ionization or/and dissociation continua, and have been analyzed by the Fano's configuration interaction theory [16] and multi-channel quantum defect theory (MQDT) [17-20]. Measuring the internal state distributions of photoproducts have also provide much information on the insight of decay process and kind of interactions including in the processes. Non-Franck-Condon distributions of vibrational state of ions have revealed the existence and significant contributions of the electronic configuration mixing of Rydberg states and the dissociative valence superexcited states [21]. Vibrational and rotational autoionization processes have been also investigated by pump-probe experiments using laser multiphoton techniques [22]. In addition, as for the direct ionization process, the rotational state distributions of N_2^+ produced by direct ionization process have been observed by HeI high resolution photoelectron spectroscopy and interpreted in terms of the rotational propensity rule for the direct ionization [23].

The neutral dissociation process from superexcited states have been studied by dispersing the fluorescence from the excited neutral fragments as a function of the excitation photon energy [24-26]. In addition, photoelectron spectroscopy as a function of photon energy of synchrotron radiation, called two-dimensional photoelectron spectroscopy (2D-PES), have also revealed the existence of the neutral dissociation process and their features [27-28]. For instance, *Hikosaka et al.* have measured the 2D-PES of OCS and suggested that there are two types of dissociation, *i.e., participant* and *spectator* neutral dissociation processes [29]. In the latter case, the principle quantum numbers of the Rydberg state do not change during neutral dissociation. Pump-probe spectroscopy using multiphoton laser excitation has been applied for measuring the yield curve of neutral fragments from superexcited NO molecules, and the Rydberg-valence interactions were discussed by the MQDT analysis [29].

However, there remain a lot of problems to be clarified for the dynamics of superexcited

states. The rotational state distributions of ions from *electronically* autoionizing state have not been observed yet to the best of our knowledge, probably because the electronically autoionizing states are located in relatively higher photon energies than the rotationally and vibrationally autoionizing Rydberg states. The rotational state distribution of ions would clarify how the autoionization is induced by configuration interaction of Rydberg states with the ionization continua or by the rotational-electronic interaction. This means that if the Rydberg states are well described by the Hund's coupling case (a) or (b), the change of the rotational quantum number of the ions are expected to be observed and it can be understood what types of the partial waves of photoelectron are more likely to couple with the core [30]. In addition, the ℓ-uncoupling [31] and the long-range interaction of Rydberg electron with the molecular rotation [1] will be clarified with respect to the symmetry and principal quantum numbers of autoionizing Rydberg states.

For the neutral fragmentation process, there has been little information on the internal state distributions. Only the case in which we can measure them has been that the neutral fragment is (super) excited, as denoted above. The neutral fragments that emit neither photoelectron nor photoemission can not be observed with an one excitation source, but such kind of "dark" neutral species are known to have significant contributions to the total neural dissociation yield [32]. Hence, detecting the internal state distribution of stable neutral fragments have also been expected. The electronic state distribution of neutral fragments will make it clear the correlation of electronic state configuration between Rydberg superexcited states and dissociative states leading to the fragments. The vibrational and rotational state distribution of the neutral fragments include information on the geometry of the potential energy surface, as investigated in the VUV region extensively [33]. In the case of the neutral dissociation from superexcited states, the electronic correlation with ionization continua may affect the neutral dissociation processes and their yields.

In addition, shape resonance observed in XUV region also provides the interesting physical systems in which a photoelectron temporary trapped in the centrifugal barrier interacts with both other electrons and ion core [1]. The decay process is sensitive to the molecular

geometry, and non-Franck-condon behavior of the vibrational state distributions and the anormal angular distributions of photoelectrons have been also observed [34]. The rotational state distributors of fragment ions will also bring us the insight of these processes.

This study shows the development of the experimental technique for measuring the internal state distributions of ions, fragment ions, and neutral fragments produced from superexcited states by means of a laser induced fluorescence (LIF) spectroscopy and a resonance enhanced multiphoton ionization (REMPI) spectroscopy combined with synchrotron radiation photoexcitation[#2]. The dispersed undulator radiation emitted from BL3A2 in the UVSOR facility was used as a pumping source. The second harmonic of a Ti:sapphire laser and excimer-pumped dye laser were used for LIF and REMPI measurement, respectively, as a probe source. Apparently, the pump-probe experiments combined with synchrotron radiation and laser have advantages in terms of measuring the internal state distribution of photoproducts compared with other conventional method such as mass spectrometry, photoelectron spectroscopy and fluorescence spectroscopy. The spectral resolution of photoelectron analyzer is limited to ~ a few meV, and then the rotational state distribution of ions is difficult to measure except the ion with a large rotational constant like H_2^+. The resolution of mass filter is not enough to resolve the rotational state distribution, either. In addition, the neutral fragments as well as fragment ions emitting neither photoelectron nor fluorescence are difficult to detect with one excitation source. Synchrotron radiation as an excitation source has also advantages over laser multi-photon excitation techniques in spite of its small photon flux. It enables us to investigate the phenomena observed in wide energy range from the outer valence to inner valence region. Measuring the internal state distributions of photoproducts also give the quantities such as the electronically, vibrationally and rotationally resolved partial cross sections in each photoproducts. These quantities can be directly compared with those calculated by theory, and in turn, the theoretical development in MQDT will be stimulated for treating the newly observed decay features of the superexcited states.

[#2]The synchrotron radiation excitation combined with LIF spectroscopy is reffered to here as SR-LIF spectroscopy, and that combined with REMPI SR-REMPI spectroscopy.

Scope for this thesis can be summarized as follows. Chapter II shows the system overview for LIF spectroscopy combined with the undulator radiation. The signal count rates are estimated as a function of the photon flux of undulator radiation when the Ti:sapphire laser and excimer pumped dye laser are used as a probe source. The LIF spectrum for the transition $N_2^+(B\ ^2\Sigma_u^+,\ v = 0) \leftarrow N_2^+(X\ ^2\Sigma_g^+,\ v = 0)$ produced from N_2 are measured with the spectral resolution of 11 and 1.4 cm^{-1} and compared its signal count rate with that calculated. In chapter III, the photodissociation and photoionization dynamics of N_2, CO, and N_2O are studied by using LIF spectroscopy. Chapter III dealing with the results and discussion are divided into four parts: In the first part, the rotational structure of the electronic transition $N_2^+(B\ ^2\Sigma_u^+,\ v' = 0) \leftarrow N_2^+(X\ ^2\Sigma_g^+,\ v'' = 0)$ formed from N_2 is measured by LIF spectroscopy with the spectral resolution of 1.6 cm^{-1}. In the second part, rotational state distribution of $CO^+(X\ ^2\Sigma^+,\ v = 0)$ produced by undulator radiation excitation of CO is measured by LIF spectroscopy. In the third part, the yield curves for the v = 0 and v = 1 vibrational levels of $N_2^+(X\ ^2\Sigma_g^+)$ produced from N_2 are measured in the range 760 - 800 Å by scanning the photon energy of the undulator radiation. In the final part of chapter III the rotational state distribution of $N_2^+(X\ ^2\Sigma_g^+,\ v = 0)$ produced by undulator radiation excitation of N_2O are measured by LIF spectroscopy and the dissociation mechanism is discussed in terms of the phase space theory and the impulsive model for unimolecular dissociation. In chapter IV, the neutral S (^3P_J) fragments produced by undulator radiation excitation of OCS are detected by REMPI spectroscopy. General conclusion is presented in chapter V.

References

[1] I. Nenner and J. A. Beswick, Chap. 6, Molecular Photodissociation and Photoionization, in Handbook on Synchrotron Radiation, *Vol 1 and 2, Elsevier Science, 1987.*

[2] For instnace, A. Zewail et al, *The Chemical Bond*, Academic Press, London, 1992.

[3] T. Mitani, H. Okamoto, Y. Takagi, M. Watanabe, K. Fukui, S. Koshihara, C. Ito, Rev. Sci. Instrum., 60 (1989) 1569.

[4] J. Lacoursieere, M. Meyer, L. Nahon, P. Morin, and M. Larzilliére, Nucl. Instr. and Meth. in Phys. Res. A351 (1994) 545; M. Meyer, L. Nahon, J. Lacoursiére, M. Gisselbrecht, P. Morin and M. Larzilliére, J. Elec. Spectrosc. and Relat. Phenom. 79 (1996) 343.

[5] J. Gatzke, R. Bellmann, I. Hertel, M. Wedowski, K. Godehusen, P. Zimmermann, T. Dohrmann, A. v.d. Borne, and B. Sonntag, Nucl. Instr. and Meth. A, 365 (1995) 603.

[6] M. Mizutani, M. Tokeshi, A. Hiraya, and K. Mitsuke, J. Synchrotron Rad. 4 (1997) 6.

[7] L. Nahon, P. Morin, M. Larzilliére and I. Nenner, J. Chem. Phys., 96 (1992) 3628.

[8] L. Nahon, L. Duffy, P. Morin, F. Combet-Farnoux, J. Trembaly, and M. Larzilliére, Phys. Rev. A, 41 (1991) 4879.

[9] J. A. R. Samson, *Techniques of Vaccum Ultraviolet Spectroscopy*, Pied Publications, Lincoln, Nebraska, 1967.

[10] N. A. Papadogiannis, B. Witzel, C. Kalpouzos, and D. Charalambidis, Phys. Rev. Lett., 83 (1999) 4289.

[11] H. Nakamura, Int. Rev. Phys. Chem., 10 (1991) 123.

[12] K. Mitsuke, S. Suzuki, T. Imamura, and I. Koyano, J. Chem. Phys., 92 (1990) 6556.

[13] A. Giusti-Suzor and Ch. Jungen, J. Chem. Phys., 80 (1984) 986.

[14] For instance, Berkowitz and J. H. Eland, J. Chem. Phys., 67 (1977) 2740, K. Mitsuke, S. Suzuki, T. Imamura and I. Koyano, J. Chem. Phys., 92 (1990) 6556; Y. Hikosaka, H. Hattrori, T. Hikida and K. Mitsuke, J. Chem. Phys., 107 (1997) 2950.

[15] J. Berkowitz, *Photoabsorption, photoionization, and photoelectron spectroscopy,* Academic Press, 1979.

[16] U. Fano, Phys. Rev. 124 (1961) 1866.

[17] M. J. Seaton, Rep. Prog. Phys., 46 (1983) 167.

[18] Ch. Jungen and O. Atabek, J. Chem. Phys., 66 (1977) 5584.

[19] H. Lefebvre-Brion, A. Giusti-Suzor and G. Raseev, J. Chem. Phys., 83 (1985) 1557.

[20] H. H. Fielding, J. Chem. Phys., 106 (1997) 6588.

[21] P. M. Guyon, T. Baer, and I. Nenner, J. Chem. Phys., 78 (1983) 3665.

[22] J.W.J. Verschuur and H. B. Van Linden Van Den Heuvell, Chem. Phys., 129 (1989) 1.

[23] P. Baltzer, L. Karlsson and B. Wannberg, Phys. Rev. A, 46 (1992) 315.

[24] M. Ukai, S. Machida, K. Kameta, M. Kitajima, N. Kouchi, Y. Hatano, and K. Ito, Phys. Rev. Lett.,74 (1995) 239.

[25] A. Tabché-Fouhaillé, M. J. Hubin-Franskin, J. P. Delwiche, H. Fröhlich, K. Ito, P. M. Guyon, and I. Nenner, J. Chem. Phys., 79 (1983) 5894.

[26] L. C. Lee, R. W. Carlson, D. L. Judge, and M. Ogawa, J, Chem. Phys., 63 (1975) 3987.

[27] A. A. Wills, A. A. Cafolla, and J. Comer, J. Phys. B: At. Mol. Opt. Phys. 24 (1991) 3989.

[28] Y. Hikosaka, H. Hattori, and K. Mitsuke, J. Chem. Phys., 110 (1999) 335.

[29] A. Fujii and N. Morita, Chem. Phys. Letters, 304 (1991) 304.

[30] A. D. Buckingham, B. J. Orr, and J. M. Sichel, Phil. Trans. Roy. Soc. Lond. A. 268 (1970) 147.

[31] U. Fano, Phys. Rev. A. 2 (1970) 353.

[32] Y. Hikosaka, H. Hattori, T. Hikida, and K. Mistuke, J. Chem. Phys., 107 (1997) 2950.

[33] R. Schinke, Ann. Rev. Phys. Chem, 39 (1988) 39.

[34] L. A. Kelly, L. M. Duffy, B. Space, E. D. Poliakoff, P. Roy, S. H. Southworth, and M. G. White, J. Chem. Phys., 90 (1989) 1544.

Chapter II

Development of Laser Induced Fluorescence (LIF) Spectroscopy Combined with Synchrotron Radiation Photoexcitation.

II-1. Introduction

This chapter presents the experimental setup for probing ions produced by undulator radiation excitation by means of laser induced fluorescence (LIF) excitation spectroscopy. The performance of the present system is tested by LIF spectra for the $N_2^+(B\ ^2\Sigma_u^+, v = 0) \leftarrow N_2^+(X\ ^2\Sigma_g^+, v = 0)$ transition produced by the undulator radiation of N_2. The count rates of LIF signal are estimated as a function of the photon flux of undulator radiation to search for the appropriate experimental condition.

II-2. Experimental Section

II-2.1. *General Features*

Figure 2-1 shows a schematic diagram of the apparatus for LIF spectroscopy combined with the synchrotron radiation photoexcitation. Laser and undulator radiation are introduced into the vacuum chamber at the end-station of BL3A2 with the configuration of counterpropagation. The polarization of the undulator radiation is parallel to that of the probe laser. Sometimes, two metal filters of Sn or Tn are introduced into the path of the undulator radiation to eliminate the higher orders of the undulator radiation from the monochromator.

Sample gases are expanded into the vacuum chamber through the multichannel capillary array plate perpendicularly to both of the light beams. The ambient pressure in the vacuum chamber is kept constant at below 1×10^{-5} Torr when the sample is introduced. Fluorescence at the right angle to the molecular beam and the two light beams is collected with achromatic lenses and dispersed with a monochromator (Ritu, MC10N, 600 grooves/ mm, f = 10 cm), and detected with a photomultiplier tube (Hamamatu, R943). The optical filter (L42, Q = 420 nm) is equipped for preventing the stray light of the probe laser from entering the monochromator.

A cylindrical ion trap (Jordan, C-1251) is introduced to increase the effective number density of ions produced by synchrotron radiation excitation. The negative pulse is applyed to the end electrode (see section II-2.4) with 400 Hz to pull out the ions from ion trap. The details of the ion trap will be presented in sec. II-2.4.

The signal output from the photomultiplier (PMT) is preamplified and fed into a constant fraction discriminator (EG&G, 473A). The lock-in detection is employed to prevent both the emission coming from the higher excited states of ions produced by synchrotron radiation excitation alone and stray scattering light of the probe laser alone. The second harmonic of the Ti:sapphire laser is shuttered by an optical chopper (Stanford Research Systems, SR540) at the repetition frequency of 400 Hz. The numbers of photons are counted

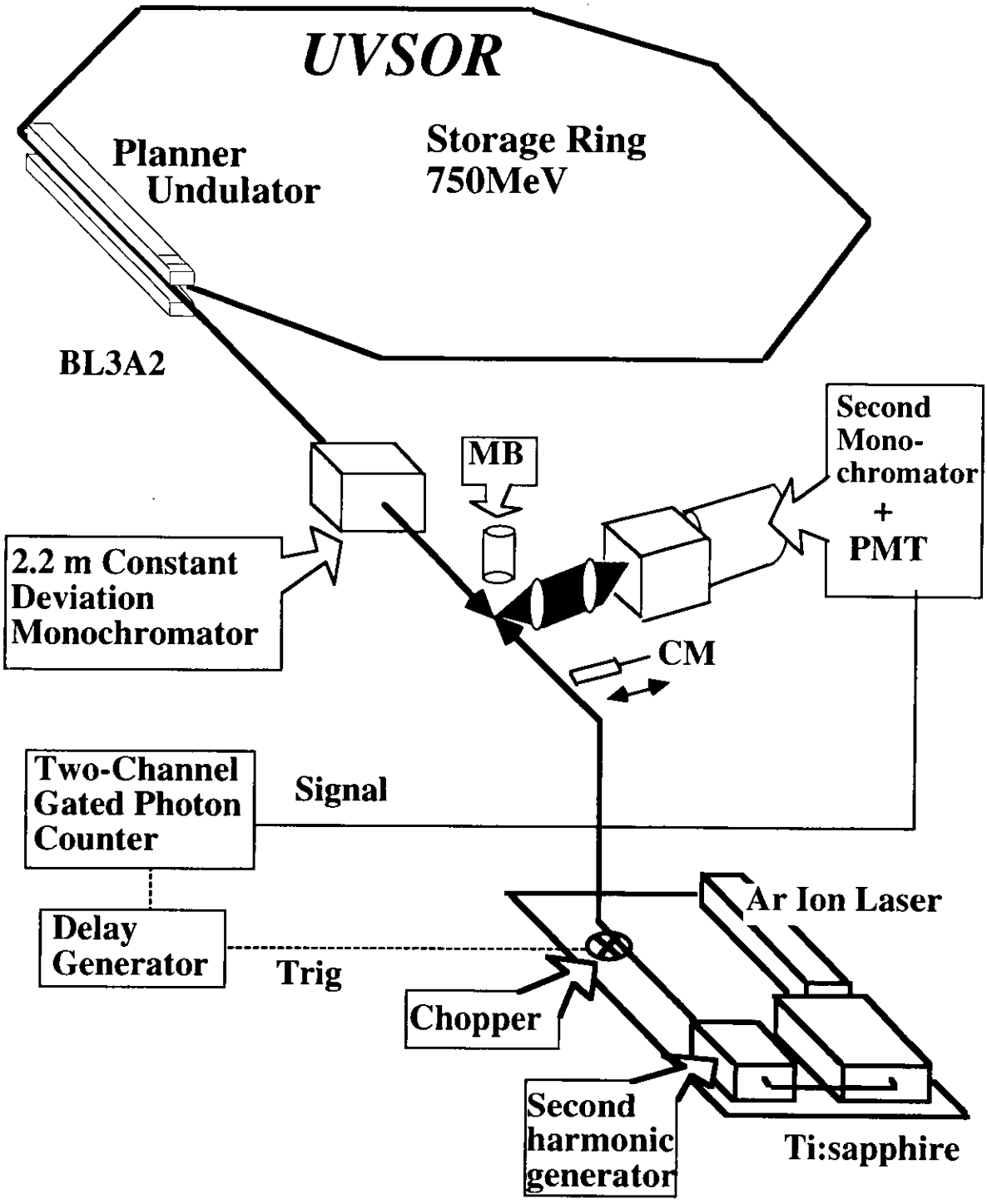

Figure 2-1. Experimental setup for the laser-synchrotron combination experiment. MB, molecular beam; CM, current monitor; PMT, photomultiplier.

separately for laser on (Channel A) and laser off (Channel B) periods by a two-channel gated photon counter (EG&G, 994). The photon counts resulting from undulator radiation excitation alone is removed by subtracting the number of photons in channel A with those in channel B (= A - B). The same measurement is repeated with the undulator radiation being shuttered, giving the signal counts A' and B', respectively, and the value A' - B' yields the number of photons due to laser scattering. The number of the photons resulting from both the undulator radiation and laser excitation is thus given by the expression (A - B) - (A' - B').

II-2.2. *Synchrotron Radiation*

Ultraviolet **S**ynchrotron **O**rbital **R**adiation (**UVSOR**) facility in IMS consists of a 15 MeV linear accelerator (liniac) as an electron beam pre-injector, a synchrotron accelerator of 600 MeV as an injector for the storage ring, and a 750 MeV electron storage ring [9]. The diagram of UVSOR is shown in Fig. 2-2 [10] The electron beam injected from the liniac and accelerated by the synchrotron accelerator is further injected into the storage ring, and accelerated up to 750 MeV. The energy of the electron beam lost by emitting synchrotron radiation is supplied by a radio-frequency (RF) cavity. When the UVSOR is operated in *multibunti* mode, the electron beams are bunched into 16 bunches, and the repetition frequency of the pulse of radiation is kept at 90.115 MHz. Main parameters of the UVSOR accelerator complex are summarized in Table 2-1.

The radiation emitted from planar-type undulator is available at beam line 3A2 (BL3A2) [10]. This type of undulator is composed of two magnetic lines, and installed in a long straight section of the UVSOR storage ring. The radiation from different periods of magnetic lines interacts coherently each other, leading to a sharp peak at fundamental undulator radiation when the deflection parameter, K, which characterizes the electron motion in a magnetic

field, is less than unity. The wavelength of the fundamental harmonic, λ_1 [Å], on axis is given by [11]

$$\lambda_1 = \frac{13.056\lambda_u}{E^2}(1 + K^2/2)$$
$$K = 0.394\lambda_u B_0 \qquad (2\text{-}1)$$

where λ_u [m] represents the length of the magnetic period, B_0 the magnetic filed strength, and E [GeV] the electron energy in the storage ring. The peak photon energy of the fundamental undulator radiation thus varies with changing the magnetic filed strength, which depends on the width of the magnetic lines. The undulator radiation is dispersed by the constant-deviation grazing-incidence monochromator with 2.2 m forcal length equipped at BL3A2 [12]. Changing three gratings, the monochromator covers the wide wavelength region 1000 - 100 Å: the grating called G1 (600 lines mm^{-1}) coveres from 953 to 225 Å, G2 (1200 lines mm^{-1}) from 538 to 124 Å, and G3 (2400 lines mm^{-1}) from 270 to 99 Å. The spectral resolution is 0.8 Å for G1, 0.4 Å for G2, and 0.2 Å for G3 per 100 μm both slit widths of the monochromator [12]. Typical dispersed spectrum of the undulator radiation is presented in Fig. 2-3. The width between the number of magnetic lines is 41.9 mm. The intensity of the radiation is measured by the gold mesh current monitor attached at the end of experimental chamber. The band width (FWHM) of the fundamental undulator radiation is approximately 1.3 eV centered at 15.84 eV, where the photon flux of the dispersed undulator radiation is attained to be 38 nA corresponding to 1.5×10^{13} photons s^{-1} mm^{-2}. A broad peak located at around 30 eV is also noticed, and ascribed to the second order of undulator radiation. The ratio of the intensity of the first to the second order lights becomes smaller with increasing photon energy.

The wavelength of the monochromator was calibrated by measuring the yield curves of N_2^+ as a function of the photon energy of undulator radiation and comparing with the reported values. The exact wavelength is given by subtracting +5.8 Å from the measured value with the accuracy of ± 0.1 Å.

Table 2-1. Main Parameters of the UVSOR Accelerator Complex [9].

Injection Linac	
Energy	15 MeV
Energy Spread	~ 1.6 MeV
Frequency	S-band 2856 MHz
Acceleration	$2\pi/3$ Traveling Wave
Length	2.5 m
Klystron Power	1.8 MW
Repetition Rate	2.6 Hz
Booster Synchrotron	
Lattice Type	FODO
Energy	600 MeV
Beam Current	32 mA (8-bunch filled)
Circumference	26.6 m
Super Cell	6
Bending Radius	1.8 m
Betatron Tune	2.25 (horizontal)
	1.25 (vertical)
Momentum Compaction	0.138
Harmonics	8
RF frequency	90.115 MHz
Repetition Rate	2.6 Hz
Storage Ring	
Lattice Type	Chasman-Green
Energy	750 MeV
Critical Energy	425 eV
Super Cell	4
Bending Radius	2.2 m
Betatron Tune	3.16 (horizontal)
	1.43 (vertical)
Momentum Comparison	0.0264
Emittance	164 nm rad (horizontal)
RF Frequency	90.115 MHz
Harmonics	16
Beam Current	
	Multi-Bunch 200 mA
	Single-Bunch 60 - 70 mA
Beam Lifetime	4 h at 200 mA
Magnetic Period (Linear Undulator)	λ_u = 8 cm

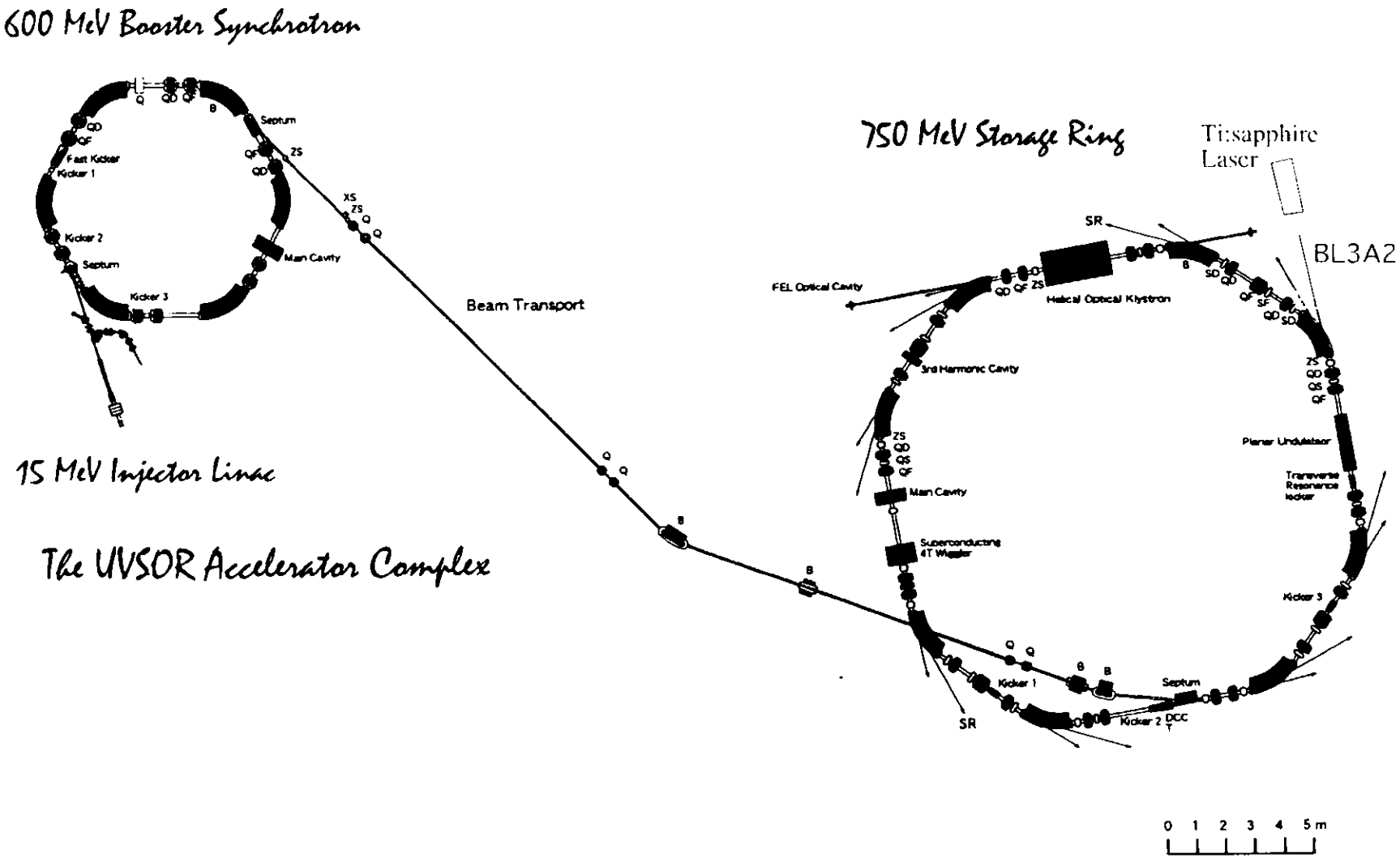

Figure 2-2. The schematic diagram of UVSOR facility in IMS [10]. The location of BL3A2 and Ti:sapphire laser are denoted in the figure.

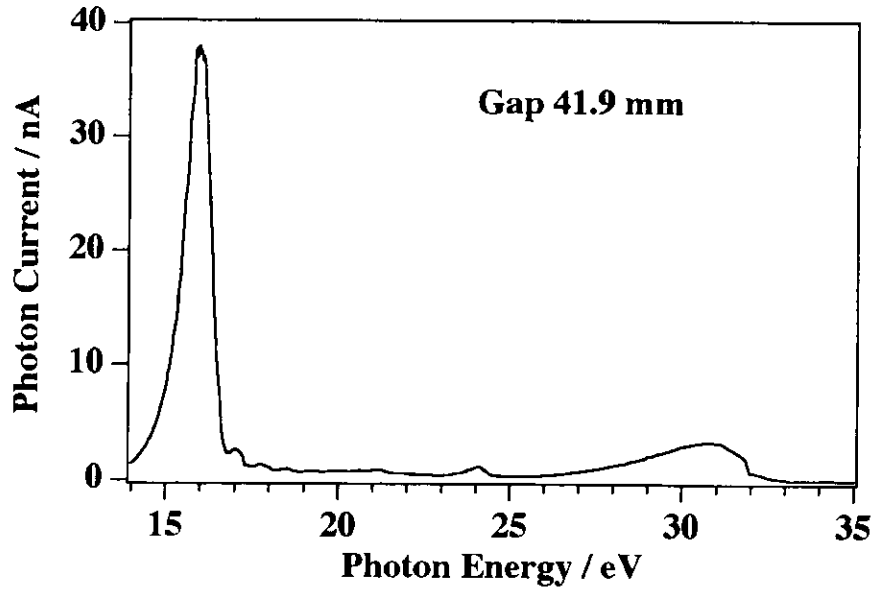

Figure 2-3. Dispersed spectrum of the undulator radiation. The width between of magnetic lines was 41.9 mm. The spectral resolution of second monochromator was 0.8 Å at ~ 15 eV.

II-2.3. *Ti:sapphire Laser*

Figure 2-4 shows the schematic overview of the cavity design of the Ti:sapphire laser (Spectra Physics Lasers, Tunami, 3950-L2S, [13]). The laser cavity is composed in M_{10} and motor-driven Gires-Tournois Interferomter (GTI). A 10 W multimode Ar^+ ion laser (Spectra Physics, Model 2060-10S) is introduced as a pump laser, and focused at the active medium of Ti:Al_2O_3(Ti:sapphire) rod with two spherical mirrors denoted by P_2 and M_3. Emission of Ti:Al_2O_3($^2E_g \rightarrow {}^2T_{2g}$) ranges from 650 to 1000 nm, and the corresponding homogeneous band width is ~100 THz [14]. The spatial distribution (transverse mode) attains to the TEM_{00} (transverse electric and magnetic wave) mode [13].

The acoust-optic modulator (AOM) is fitted in the laser cavity and driven at 90.115 MHz for the active mode locking of the Ti:sapphire laser [15]. The repetition rate of the mode-locked pulses can be completely synchronized with those of the external pulse source by changing the laser cavity length [13]. This is performed automatically by stabilizing the laser pulse by the use of an electronic module providing phase-locked loop (*Spectra physics, Lock-to-Clock, Model 3930*) [16]. For instance, we can make the laser repetition rate agree with that of the synchrotron radiation in UVSOR in the multimode operation mode [1]. The wavelength of Ti: sapphire laser is selected in the range 720 - 840 nm by manipulating the angle of birefringent filter (*BRF*). The exact wavelength is determined by use of the wavemeter (*ILX Light Wave, LMW6500B*) with the accuracy of ± 0.02 nm.

We can use two types of GTI, one generates long pulses and the other short pulses. Respective temporal pulse widths, Δt (FWHM) are determined by scanning autocorrelator (*Spectra Physics model 409*) to be 8.8 ps (longer pulse) and 1.5 ps (shorter pulse). Assuming a chirp-free $sech^2$ profile, the associated spectral band width of $\Delta\nu$ (FWHM) is given by [17]

$$\Delta t \times \Delta \nu = 0.32. \qquad (2\text{-}2)$$

Thus the spectral band width is estimated to be 7.1 cm^{-1} or 1.2 cm^{-1} corresponding to the 1.5 ps or 8.8 ps temporal pulse, respectively. The pulse width of the second harmonic light is

also estimatd to be 11 cm^{-1} and 1.9 cm^{-1}, respetively, from the fact that the temporal pulse width is spread by a factor of 1.55 after introducing the crystals for second harmonic generation [17].

Frequency doubling is perfomed by introducing the output of Ti:sapphire laser in a β - BaB_2O_4 (BBO) crystal [18]. By verifying the incident angle of the crystal to the direction of the fundamental light, the conversion efficiency is maximized at a given fundamental wavelength. The third harmonic can be generated by introducing both fundamental and second harmonic light to another BBO crystal. The polarization of the electric vector $\boldsymbol{E}$ of fundamental light is vertical to the ground, and that of second and third harmonic is parallel and vertical, respectively, to the ground. Table 2-2 summarizes the tunable wavelength range for the fundamental, second, and third harmonic light as well as the typical output power.

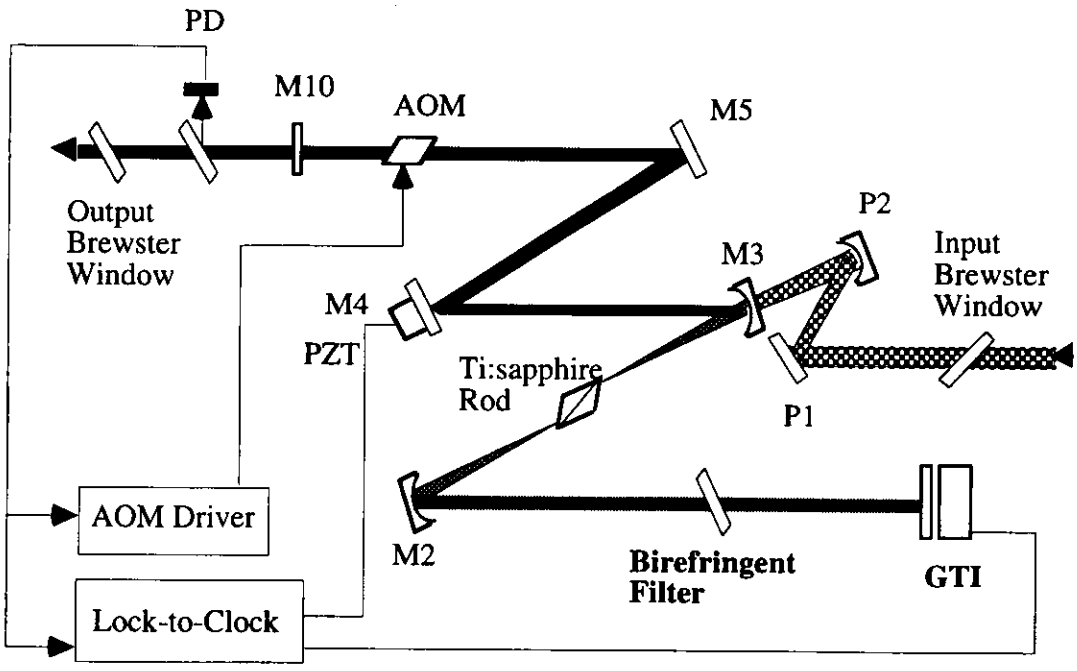

Figure 2-4. Cavity design of *Tunami*. AOM: Acousto-optic modulator; PD, photodiode; GTI, Gires-Tournois Interferomter.

Table 2-2. Tuning range of Ti:sapphire laser.

	Tuning Range	Output
Fundamental	720 - 850 nm	1.3 W
Second Harmonic[#1]	360 - 425 nm	150 mW
Third Harmonic[#1]	240 - 275 nm	50 mW

[#1] The shorter pulse is used.

II-2.4. *Cylindrical Ion Trap*

The cylindrical ion trap invoked in molecular spectroscopy has been described in detail by several groups [19-20]. A brief description is given below. A typical ion trap cell consists of two end electrodes and one central ring electrod. Applying the appropriate DC and radio frequency (*RF*) voltage to these electrodes, hyperbolic electric filed can be generated in the ion trap. The motions of ions in the field is given by Mathiueu equations [20]

$$\begin{aligned} \frac{d^2r}{dt^2} + \left(\frac{e}{mr_0^2}\right)(U + V\cos wt)r = 0 \\ \frac{d^2z}{dt^2} - \left(\frac{e}{mr_0^2}\right)(U + V\cos wt)r = 0 \end{aligned} \qquad (2\text{-}3)$$

where r and z represent the radial and axial coordinates, respectively, r_0 the inside diameter of the cell, m the mass of ions, w the frequency of *RF* voltage, and U and V are the *RF* and *DC* bias voltage applied to the cell. Ions can be trapped in the area that defined by the value of U and V when the value of w and r_0 are fixed. The maximum potential depth made by the applied voltage in the trap is given by [20]

$$D = \frac{mw}{8e}\left(\beta_r^2 r_0^2 + \beta_z^2 z_0^2\right) \qquad (2\text{-}4)$$

where β_z and β_r represent the geometry factors, which are written as [20]

$$\beta_z = a_z + q_z^2/2,\ \beta_r = a_r + q_r^2/2$$

and

$$\begin{aligned} a_z &= -\frac{1}{2}a_r = \frac{8eU}{mr_0^2w^2} \\ q_z &= -\frac{1}{2}q_r = \frac{4eV}{mr_0^2w^2}. \end{aligned} \qquad (2\text{-}5)$$

Both the maximum number of ions that can be trapped in the cell and the spatial distribution of ions can be estimated from D under the thermal equilibrium condition [20].

The schematic diagram of the cylindrical ion trap (*Jordan Company*) employed in the present study is shown in figure 2-5. The dispersed undulator radiation and laser were introduced through the apertures drilled through the central ring electrode, and the sample gas was introduced through the aperture in the end electrode. The RF voltage from the voltage supplier (*Jordan Company*) was applied to the center electrode in the range 0 - 500 V. In this trap, the geometry factors of β_z and β_r are 0.24 and 0.13, respectively, using r_0 = 10 mm, z_0 = 7.03 mm, V = 100 V and $w/2\pi$ = 1 MHz. The maximum potential depth is calculated under this condition to be ~ 6.3 eV.

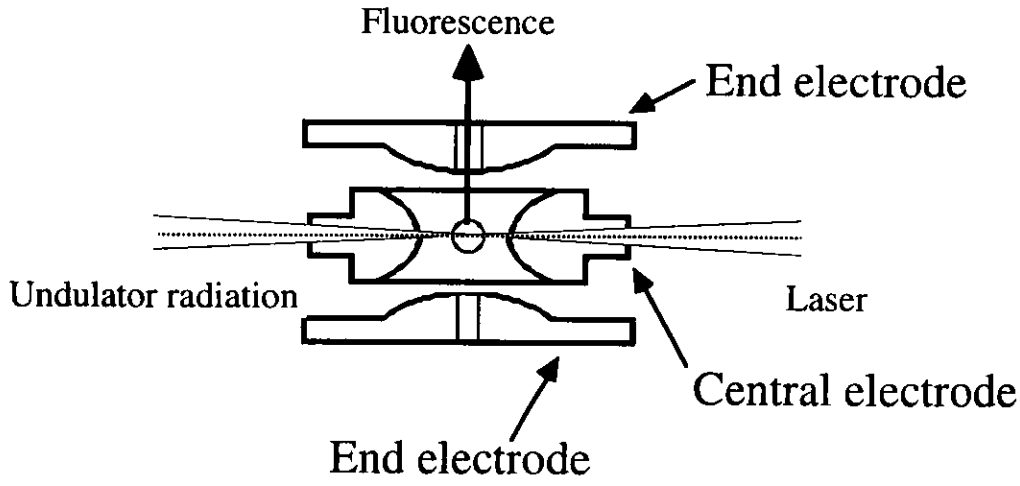

Figure 2-5. The schematic design of the ion trap cell. Ion trap is composed of an end electrode, central electrode, and end electrode.

II-3. Results and Discussion

Figure 2-6 (a) shows an LIF spectrum of $N_2^+(X\ ^2\Sigma_g^+, v, N)$ produced by the undulator radiation photoexcitation of N_2 at the photon energy of undulator radiation, E_{SR}, = 15.983 eV. This excitation energy is equal to that between the electronically ground state, $N_2(X^2\Sigma_g^+)$, and the $4d\sigma_g$ Rydberg series converging to $N_2^+(A\ ^2\Pi_u, v = 0)$ [21]. The shorter type of GTI was used and its spectral resolution is 11 cm^{-1}. Fluorescence around 427.8 nm was dispersed by a monochromator to observe the transition $B^2\Sigma_u^+, v' = 0 \rightarrow X^2\Sigma_g^+, v'' = 1$ [22]. The fluorescence signal was accumulated during 500 seconds at each laser wavelength. The fluorescence intensity maximum centered at 391.4 nm is ascribed to the *P*-branch for the electronic transition $N_2^+(B^2\Sigma_u^+, v = 0) \leftarrow N_2^+(X^2\Sigma_g^+, v = 0)$, and the signal count rate at 391.4 nm was 2 cps. The solid curve represent the calculated spectra with the rotational temperature of 300 K assuming the Bolzmann distribution in $N_2^+(X^2\Sigma_g^+, v = 0)$. The process of the calculation will be described in the next chapter.

The signal count rate is calculated for LIF spectroscopy of N_2^+ produced by undulator radiation as a function of the photon flux for comparing with the observed rate. The number of ions in a unit volume, n_{SR} [molecules cm^{-3}], produced by a pulse of the undulator radiation excitation is given by

$$n_{SR} = \sigma I_{SR} n_0 \qquad (2\text{-}6)$$

where σ_{SR}[cm^2] represents the ionization cross section of N_2, I_{SR} the number of photon in a undulator radiation pulse [photons cm^{-2} $pulse^{-1}$], and n_0 the numbers of molecules in a unit volume [molecules cm^{-3}] in the electronically ground state under a given sample pressure.

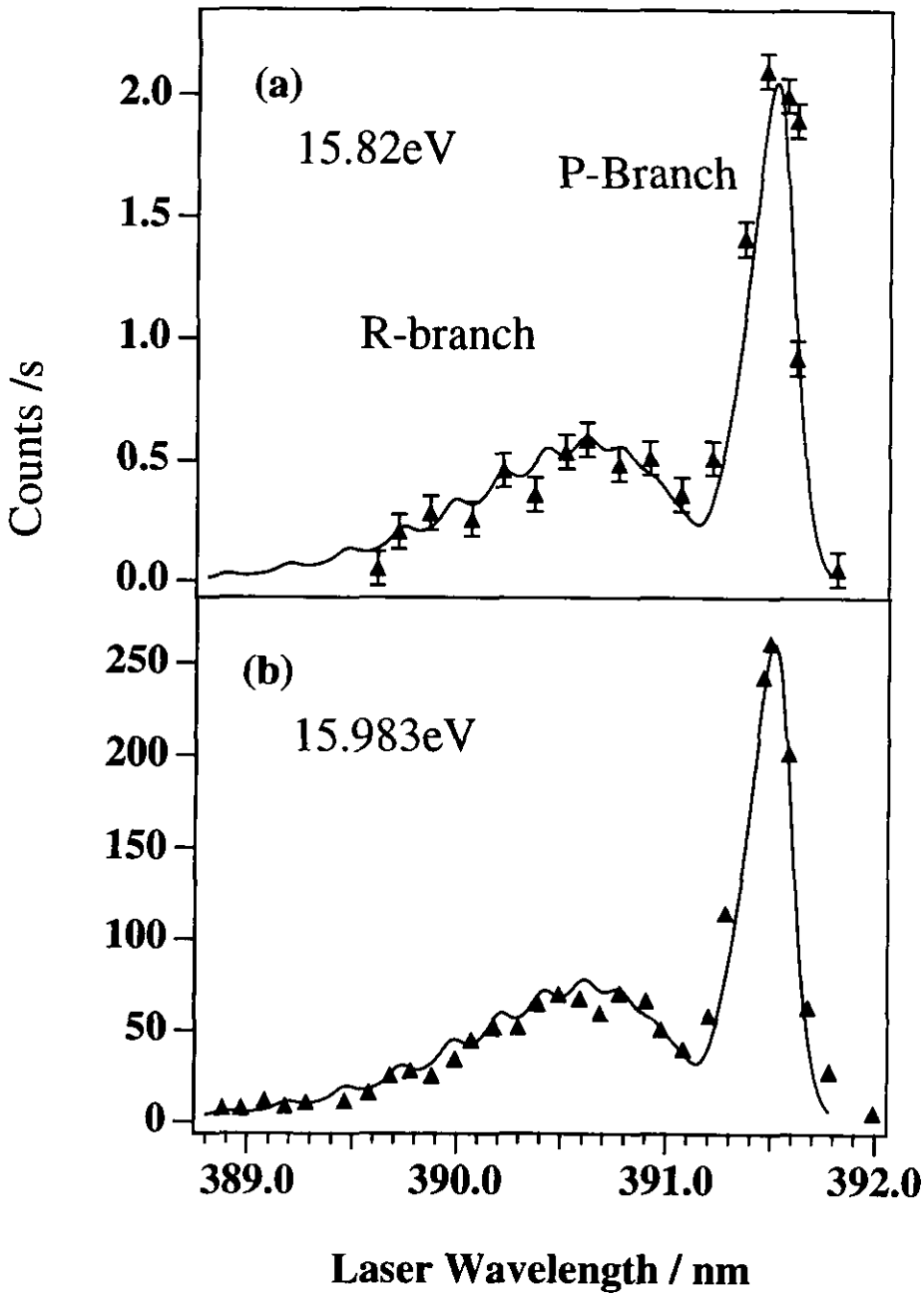

Figure 2-6. LIF spectra of the $B\,^2\Sigma_u^+$, v' = 0, N' ← $X\,^2\Sigma_g^+$, v" = 0, N" excitation of N_2^+ produced from N_2 (a) without and (b) with the ion trap. The excitation energies of the undulator radiation are (a) 15.82 eV (b) 15.983 eV respectively. The spectral resolution of the probe laser is 11 cm^{-1}. The solid lines represent the calculated curves with the rotational temperature of 300 K.

The number of $N_2^+(B^2\Sigma_u^+, v = 0)$ ions in a unit volume produced by the excitation of a single laser pulse is given by

$$n_{LR} = \sigma_{LR} I_{LR} n_{SR} f_1 f_2 f_3 \qquad (2\text{-}7)$$

where σ_{LR}[cm^2] represents the cross section for the transition $N_2^+(B\ ^2\Sigma_u^+, v = 0) \leftarrow N_2^+(X\ ^2\Sigma_g^+, v = 0)$, and I_{LR}[photons s^{-1} cm^{-2}] the number of photon in one laser pulse. The value of f_1 is given by

$$f_1 = \tau / \tau_{SR} = \tau F_{SR} \qquad (2\text{-}8)$$

where τ represents the residence time in the excitation volume, which is calculated by the thermal velocity of the ions and the beam radius of the probe laser[#1]. τ_{SR} is the repetition period of the undulator radiation, ~11ns, and is replaced by $1/F_{SR}$, that is the frequency of the undulator radiation. f_2 represents the branching ratio for the rotational state J'' of $N_2^+(X\ ^2\Sigma_g^+, v=0)$, and f_3 represents the ratio of the spectral band width of the probe laser to that of the doppler width of a single rotational line. Finally, the signal count rate, cps[s^{-1}], is given by

$$cps[s^{-1}] = n_{LR} \gamma_1 \gamma_2 \phi V F_{LR} \qquad (2\text{-}9)$$

where γ_1 represents the efficiencies determined by the geometry of the collimated optics, γ_2 the quantum efficiency of the photomultiplier, ϕ the branching ratio corresponding to the emission $N_2^+(B\ ^2\Sigma_u^+, v = 0) \rightarrow N_2^+(X\ ^2\Sigma_g^+, v = 0)$ transition, V the reaction volume, and F_{LR} the repetition rate of the probe laser.

Figure 2-7 shows the calculated signal count rates as a function of the photon flux of the dispersed undulator radiation by using the Ti:sapphire laser (upper line) and excimer pumped dye laser (lower line) as a probe laser, respectively. The average power of the

[#1] If the lifetime in the electronic states of ions is smaller than the value of τ, τ in Eq. 2-8 should be replaced by the lifetime. In the prsent case, the lifetime of $N_2(X^2\Sigma_g^+)$ is much larger than the value of τ.

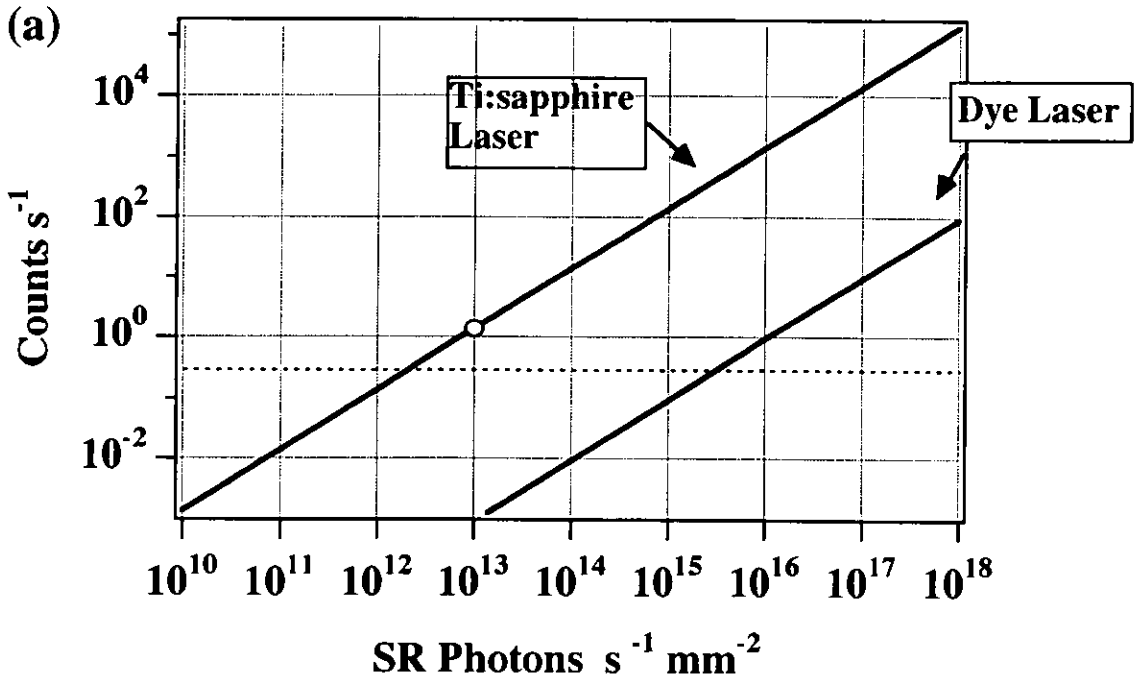

Figure 2-7. Signal count rate of N_2^+ using Ti:sapphire (upper line) and excimer pumped dye laser (lower line) as a function of the photon flux [photons s^{-1} mm^2] of the undulator radiation. Open circle correspond to the photon flux of the dispersed undulator radiation of BL3A2 of 8×10^{12} photons s^{-1} mm^{-2}.

Table 2-3 Parameters for calculating the signal count rate.

(a) Repetition Frequencies, photon flux, and beams size of undulator, Ti: Sapphire and Dye laser.

		Undulator	Ti:Sapphire	Dye
Frequencies		90.115 MHz	90.115 MHz	10 Hz
Photon flux		20 nA	100 mW	10 mJ
Beam Size		1 mm^2	1 mm^2	1 mm^2
Photon flux	[Photons cm^{-2} s^{-1}]	8×10^{14}	10^{19}	10^{19}
	[Photons mm^{-2} s^{-1}]	8×10^{12}	10^{17}	10^{17}
	[Photons cm^{-2} $pulse^{-1}$]	8×10^{6}	10^{11}	10^{17}

(b) Parameters for calculating the signal count rates.

Parameters	Values
f_1	$(2 \times 10^{-6}) \times (90.115 \times 10^{6})$
f_2	0.108 (for Ti:sapphire), 1 (for excimer pumped dye laser)
f_3	0.06 / 10
γ_1	10^{-1}
γ_2	10^{-3}
ϕ	0.24
V	1 mm^3

second harmonic of Ti:sapphire laser is taken to 100 mW, while the pulse energy of the excimer pumped dye laser is 10 mJ at the repetition rate of 10 Hz. The ionization cross section for $N_2^+(B^2\Sigma_u^+, v = 0) \leftarrow N_2^+(X^2\Sigma_g^+, v = 0)$ was assumed to the $\sigma_{SR} = 10 \times 10^{-13}$ [cm^2] (= 10^5 MB) [22]. Other parameters for the calculation are given in Table 2-3. The dotted line, where signal count rate is 0.3 cps, represents the minimum signal counts that we can recognize as a signal. This value was determined from the count rate of noise in the present system of ~ 0.1 cps. The open circle on the upper line indicates the corresponding signal count rate, 2 cps, when the photon flux of dispersed undulator radiation is 8×10^{14} photons s^{-1} cm^{-1} with a spectral resolution of 0.8Å. This is larger than that of the minimum signal counts, and therefore we confirm that the fluorescence counts are detectable observed in this experimental setup. On the other hand, the lower line in Fig. 2-7(a) indicates that we will not able to detect the fluorescence signal if we use the excimer pumped dye laser at the same undulator photon flux. This difference between the two probe light sources results from the fact that the values of $\sigma_{LR}I_{LR}$ for the dye laser is saturated to be unity at a much lower repetition frequency of 10 Hz. In contrast the value for Ti:sapphire laser is 0.02 at the repetition frequency of ~ 90.115 MHz.

Figure 2-6 (b) shows an LIF spectrum of the transition $N_2^+(B\ ^2\Sigma_u^+, v = 0) \leftarrow N_2^+(X\ ^2\Sigma_g^+, v = 0)$ with the ion trap. The amplitude of the AC voltage applied in the electrode of the ion trap was set to 100 $V_{pk\text{-}pk}$. The ambient pressure was kept to 8×10^6 Torr. Applying negative pulse at one of the end electrode with the repetition rate of 400 Hz, we pulled out the ions trapped in the cell. The fluorescence signal counts are 140 times as high as those without the ion trap. This is obviously due to the increase of the number of ions in the probing volume. The rotational temperature of $N_2^+(X\ ^2\Sigma_g^+, v = 0)$ was determined to be 300 K. Although the LIF spectrum seems to have the same envelope as that without the ion trap, one mat suspect that the rotational state distribution of $N_2^+(X^2\Sigma_g^+, v = 0)$ is affected by collisions between N_2^+ and neutral N_2 in the ion trap. For checking it, the number of N_2^+

produced in the trap was estimated. The number of N_2^+ was calculated by the equation (2-6) to be 1×10^7 ions s^{-1} under the ambient pressure of 8×10^{-6} Torr, the photon flux of 8×10^{14} photons s^{-1} cm^{-2}, and the ionization volume of 1 mm^3. If ions are keeping trapped in the cell until the negative pulse of 400 Hz is applied for sweeping away ions, the N_2^+ ions to the number of 5×10^3 are trapped in the volume of 1 mm^3 during 2.5 ms. In the ion trap this ion cloud are distributed in the volume ~ $(4\ mm)^3$ [23], the number density of ions is 8×10^{10} [ions m^3]. The number of collisions, Z, of N_2^+ with one N_2 molecule is given by [24]

$$Z = \sigma \bar{c} N_{ion} \qquad (2\text{-}10)$$

where σ_c represents the total collision cross section, $\bar{c}$ the mean speed of molecules, N_{ion} the number of ions. Assuming the thermal distribution of N_2 and $\sigma_c = 0.43$ nm^2, the number of collisions during 2.5 ms is ~ 4×10^{-8}. Then the total collision number is estimated to be ~ 140 by multiplying the number of N_2 molecules introducing into 2 mm^3 diameter on the ion trap cell, which is estimated to be 3.2×10^9 [molecules]. This suggests that about 3 % of N_2^+ molecules are subjected to collisions with neutral N_2 inside the cell. The mutual collisions of N_2^+ can be disregarded because of its low number density. The collision effect on the observed LIF spectrum will be discussed again in the following section.

It is informative to know what kind of molecules can be detected by this combination experiments. Fig. 2-8 shows the signal count rate as a function of σ_{LR} assuming the ionization cross section, σ_{SR} to be 10 Mb. Solid and broken line represent the count rate with and without the ion trap, respectively. The open circle denotes the cross section of transition the $N_2^+(B^2\Sigma_u^+,\ v = 0) \leftarrow N_2^+(X^2\Sigma_g^+,\ v = 0)$, *i.e.*, 10^5 Mb. This figure shows difficulties in observing the LIF spectrum of ions whose transition cross section is lower than ~ 5×10^4 Mb without the ion trap. Then, it is clear that we have to employ the ion trap for measuring the $CO^+(A\ ^2\Pi) \leftarrow CO^+(X\ ^2\Sigma^+)$ transition, since the cross section for the Σ - Π transition is usually much smaller than that of the Σ - Σ electronic transition [25]. The detailed discussion about the LIF spectrum of CO^+ will be presented in the next chapter.

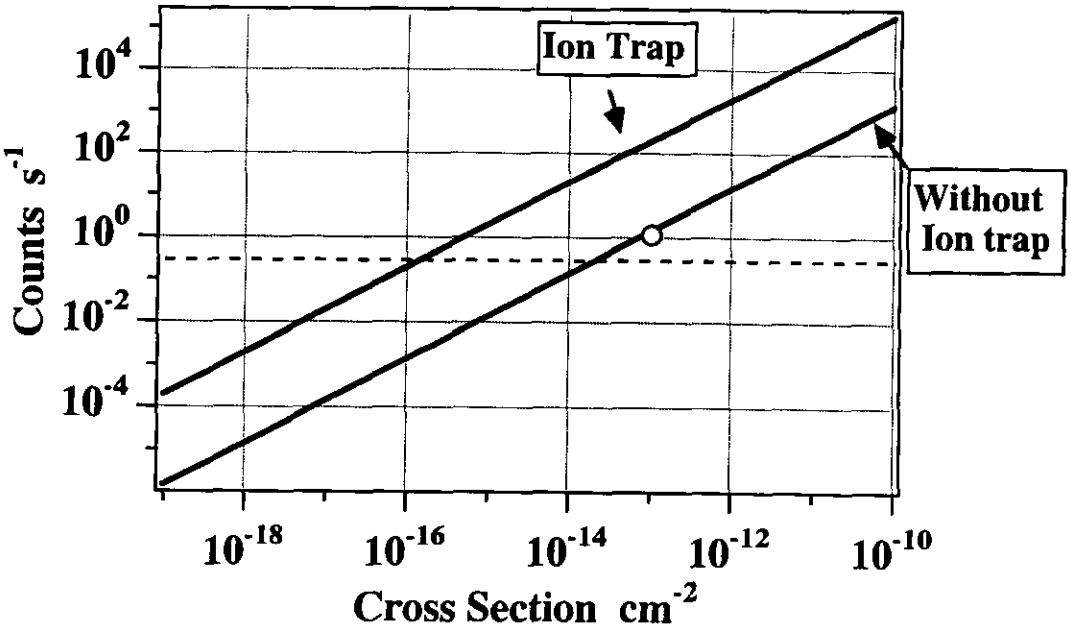

Figure 2-8. Signal count rate as a function of the cross section of ions with (upper line) and without (lower line) the ion trap (see text). Ti:sapphire laser is used as a probe source. Open circle corresponds to the value for 10^5 Mb, which corresponds to the electronic transition $N_2^+(B\ ^2\Sigma_u^+, v = 0) \leftarrow N_2^+(X\ ^2\Sigma_g^+, v = 0)$.

II-4. Conclusion

This chapter shows the experimental details for LIF spectroscopy combined with undulator radiation excitation. The N_2^+ ($X\ ^2\Sigma_g^+$, v = 0) produced by the undulator radiation excitation of N_2 is observed by means of LIF spectroscopy. The Ti:sapphire laser is expected to be very suitable to the probe laser rather than the excimer-pumped dye laser. When the cylindrical ion trap is used, the signal rate is found to be increased by a factor of 140. The calculated signal count rate shown in Fig. 2-7 and Fig. 2-8 is consistent with the observed fluorescence count rate. These sorts of calculation are useful for knowing how many signal counts are expected under particular experimental conditions.

References

[1] M. Mizutani, M. Tokeshi, A. Hiraya and K. Mitsuke, J. Synchrotron rad. 4 (1997) 6.

[2] J. Lacoursiére, M. Meyer, L. Nahon, P. Morin and M. Larzilliére, Nucl. Instr. and Meth. , A 351 (1994) 545.

[3] M. Meyer, L. Nahon, J. Lacoursiére, M Gisselbrecht, P. Morin and M Larzilliére, J. Elec. Spectrosc. and Relat. Phenom., 79 (1996) 343.

[4] J. Gatzke, R. Bellmann, I. Hertel, M. Wedowski, K. Godehusen, P. Zimmermann, T. Dohrmann, A. v.d. Borne and B. Sonntag, Nucl. Instr. and Meth, A 365 (1995) 603.

[5] M. Mitsuke, Y. Hikosaka and K. Iwasaki, J. Phys. B, in press.

[6] L. Nahon, L. Duffy, P. Morin, F. Combet-Farnoux, J. Tremblay and M. Larzilliére, Phys. Rev. A, 41 (1990) 4879.

[7] L. Nahon, A. Svensson and P. Morin, Phys. Rev. A, 43 (1991) 2328.

[8] L. Nahon, P. Morin, M. Larzilliére and I. Nenner, J. Chem. Phys., 96 (1992) 3628.

[9] UVSOR activity report, 1999.

[10] H. Hama, private communication.

[11] *X-ray data booklet, D. Vaughan, 1986.*

[12] E. Ishigro, M. Suzui, J. Yamazaki, E. Nakamura, K. Sakai, O. Matsudo, N. Mizutani, K. Fukui and M. Watanabe, Rev. Sci. Instrum, 60 (1989) 2105.

[13] *Spectra Physics, Tunami, manual.*

[14] B. E. A. Saleh and M. C. Teich, *Fundermentals of Photonics,* 1988, *Wiley.*

[15] M. J. W. Rodwell, D. M. Bloom and K. J. Weingarten, IEEE J. Quantum Electronics, 25 (1989) 817.

[16] D. E. Spence, P. N. Kean and W. Sibbett, Optics Letters, 16 (1991) 42.

[17] A. Nebel and R. Beigang, Optical Letters, 16 (1991) 1729.

[18] W. H. Glenn, IEEE J. Quantum Electronics, 6, (1969) 284.

[19] N. Mikami, A. Okabe and I. Suzuki, J. Phys. Chem., 92 (1988) 1858.

[20] J. Yoda, Jpn. App. Phys., 49 (1980) 802.

[21] H. Lefebvre-Brion and K. Yoshino, J. Mol. Spec., 158 (1993) 140.

[22] A. Lofthus and P. H. Krupenie, J. Chem. Phys. Ref. data, 6 (1977) 113.

[23] H. Schaaf, U. Schmeling, and G. Werth, Appl. Phys. 25 (1981) 249.

[24] P.W. Atkins, *Physical Chemistry 5th,* Oxford Press, London, 1995.

[24] G. Herzberg, Molecular Spectra and Molecular Structure, I. Spectra of Diatomic Molecules ; Van Nostrand: New York, 1966.

Chapter III

LIF Spectroscopy of Ions Produced by Synchrotron Radiation Photoexcitation *(Chemical Physics Letters, 317 (2000) 45)*

III-1. Introduction

This chapter describes LIF spectroscopy of ions and fragment ions formed by undulator radiation excitation. The rotational state distribution of $N_2^+(X\,^2\Sigma_g^+, v = 0)$ formed by undulator radiation excitation were measured by using LIF spectroscopy in the spectral resolution of 1.6 cm^{-1} and 11 cm^{-1}. A schematic energy diagram of the electronic states of N_2 and N_2^+ is shown in Figure 3-1 with photoexcitation and probing pathway. The yield curves for the v = 0 and v = 1 vibrational levels of $N_2^+(X\,^2\Sigma_g^+)$ were measured in the range 760 - 800 Å by observing the LIF intensity at a fixed laser wavelength. The rotational state distribution of $N_2^+(X\,^2\Sigma_g^+, v = 0)$ formed by the undulator radiation excitation of N_2O was measured at the photon energy of 17 - 35 eV. The dissociation mechanism is discussed by using the statistical phase space theory and the modified impulsive model for unimolecular dissociation.

III-2. Experimental Section

The experimental details for LIF spectroscopy is described in the previous chapter. An ion trap was employed in the measurement that perfomed in this section. Gaseous N_2 (Nihon Sanso, 99.9995%), N_2O (Showa Denko, 99.99 %) and CO (Nihon Sanso, 99.99%) were used without further purification.

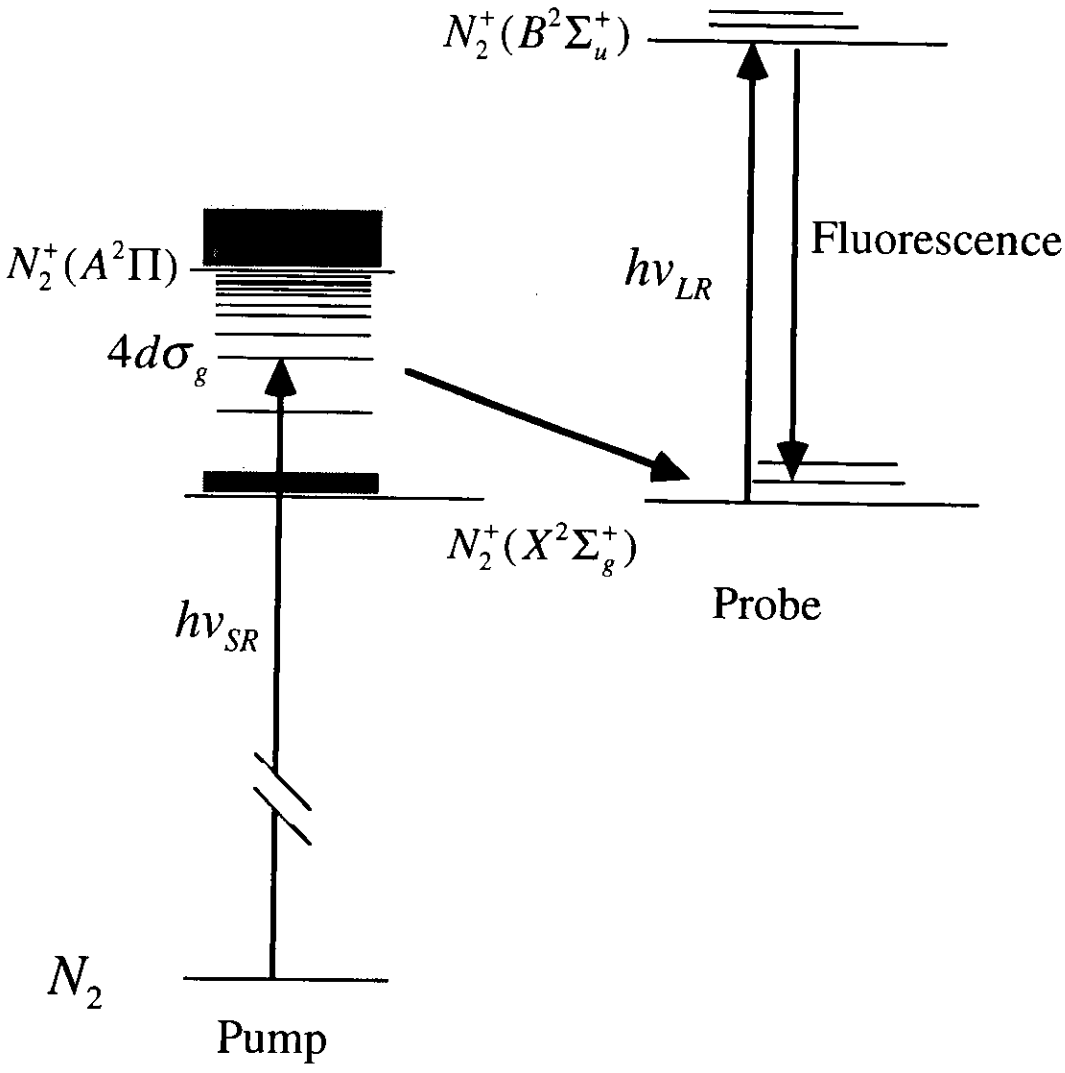

Figure 3-1. A schematic energy diagram of the electronic states of N_2 and N_2^+ with photoexcitation and probing pathway. $h\nu_{SR}$ and $h\nu_{LR}$ represent the photon energy of the undulator radiation and the laser, respectively.

III-3. Results and Discussion

III-3.1. LIF spectrum of $N_2^+(X\,^2\Sigma_g^+, v = 0, N)$

Figure 3-2 (a) shows an LIF spectrum of $N_2^+(X\,^2\Sigma_g^+, v, N)$ produced by the photoexcitation of N_2 with undulator radiation. The photon energy was fixed at E_{SR} = 15.983 eV, which is equal to the excitation energy of the $4d\sigma_g\ ^1\Pi_u$ Rydberg state converging to $N_2^+(A\,^2\Pi_u, v = 0)$. Fluorescence was dispersed by the monochromator at the wavelength of 427.8 nm corresponding to the transition $B\,^2\Sigma_u^+, v' = 0 \rightarrow X\,^2\Sigma_g^+, v'' = 1$. The longer pulse was chosen to obtain a better spectral resolution of the probe laser. The spectral resolution of 1.6 cm^{-1} (0.2 meV) is much better than that achieved by a conventional photoelectron spectroscopy [1-2].

We can clearly resolve the rotational structures of the *R*-branch corresponding to the electronic transition of $N_2^+(B\,^2\Sigma_u^+, v' = 0, N') \leftarrow N_2^+(X\,^2\Sigma_g^+, v'' = 0, N'')$. The alternation of the intensities of the rotational lines is observed, which results from the difference in the degeneracy of the nuclear spin of homonuclear diatomic molecules [3-4]. The rotational structures of the *P*-branch are overlapped because of the reversal of the rotational lines.

The energy of the rotational level for $N_2^+(X\,^2\Sigma_g^+, v = 0)$ and $N_2^+(B^2\Sigma_u^+, v = 0)$, *F(N)*, is given by [3]

$$F(N) = \nu_0 + BN(N+1) - DN^2(N+1)^2 + \ldots \qquad (3\text{-}1)$$

where ν_0 represents the vibronic energy measured from the neutral ground states, *B* is the rotational constant and *D* is the centrifugal distortion constant of $N_2^+(X\,^2\Sigma_g^+, v = 0)$ or $N_2^+(B\,^2\Sigma_u^+, v = 0)$, respectively. These molecular constants are summarized in Table 3-1 [3, 5]. The excitation energy of an individual rotational line is calculated from Eq. (3-1) for *P* and *R* branches.

The relative intensities of the individual rotational lines in the LIF spectrum can be given by

$$I_{N''N'} \propto g_{N''} S_{N''N'} \exp(-hcB''N''(N''+1)/kT), \qquad (3\text{-}2)$$

where $g_{N''}$ is the statistical weight due to the nuclear spin, $S_{N''N'}$ is the Hönl-London factor for the Σ - Σ transition. The rotational state distribution of N_2^+ ($X\ ^2\Sigma_g^+$, v" = 0, N") is assumed to obey the Boltzmann distribution at a temperature, T.

Next, I measured the LIF spectrum of $N_2^+(X\ ^2\Sigma_g^+$, v = 0) with a low spectral resolution in order to determine the exact rotational temperature. The rotational structures in the P and R branches become entirely overlapped. Two excitation photon energies are selected: 15.983 eV (on resonance with the $4d\sigma_g$ Rydberg state) and 15.870 eV (off resonance). At both photon energies the rotational temperature of $N_2^+(X\ ^2\Sigma_g^+$, v = 0) is evaluated to 300 K by fitting the observed data points with the theoretical intensity distribution of Eq. (3-2) convoluted with the sech^2 function of FWHM = 11 cm^{-1}.

The rotational quantum number, N, of N_2^+ can vary during the direct ionization or autoionization processes [6-8]. For direct ionization of $N_2(X\ ^1\Sigma_g^+)$ to $N_2^+(X\ ^2\Sigma_g^+)$, a ΔN = 0, ±2 and ±4 propensity rule has been proposed from the results of high-resolution photoelectron spectroscopy [4]. Though a propensity rule for the electronic autoionization from $4d\sigma_g$ state would be different from that for direct ionization, no significant difference in the rotational temperature was observed in the present study. This may be attributed to that the initial rotational temperature of N_2 is too high to distinguish a small change in the rotational quantum number between $N_2^+(X\ ^2\Sigma_g^+$, v = 0) and $N_2(X\ ^1\Sigma_g^+$, v = 0) caused by electronic autoionization.

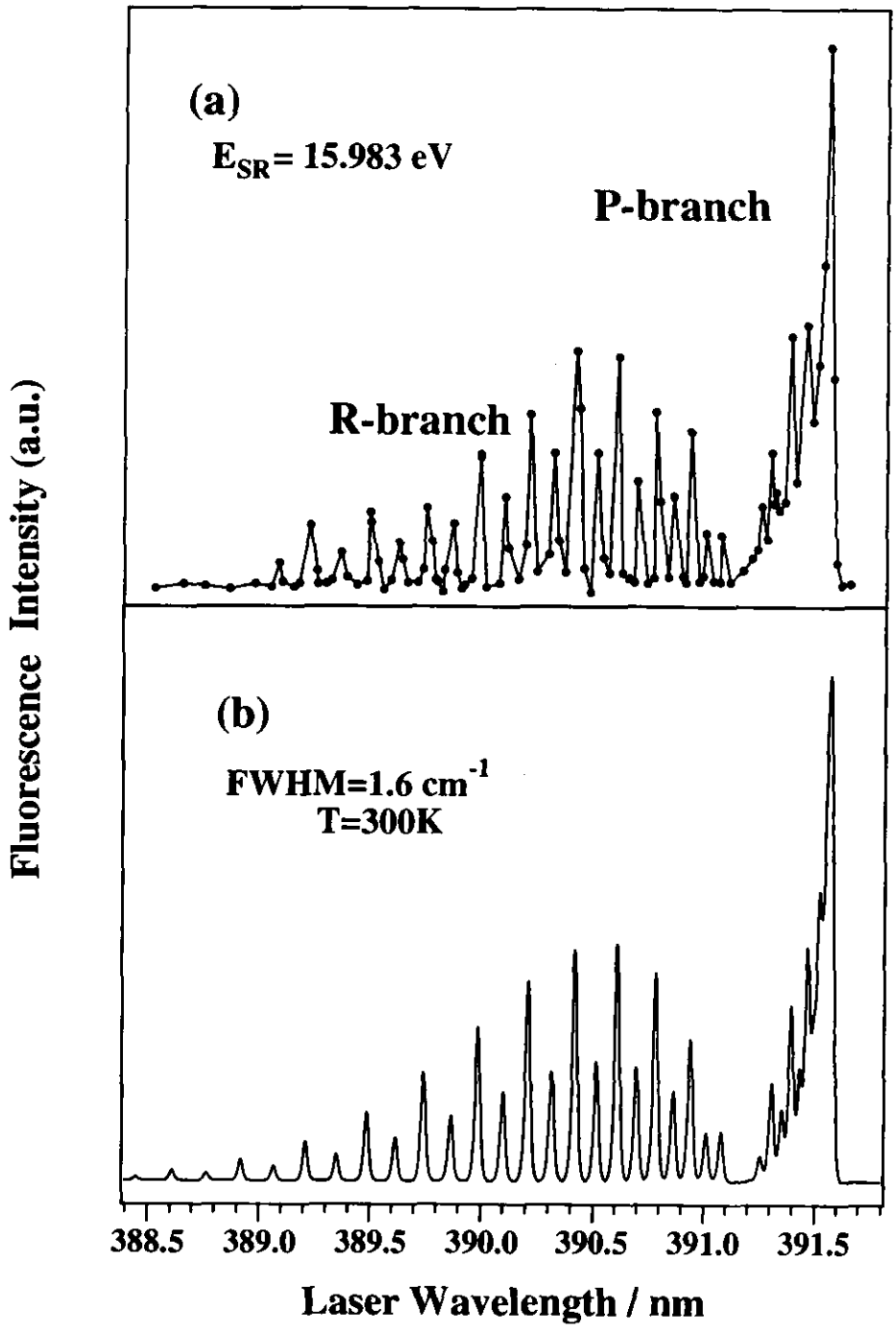

Figure 3-2. (a) Observed and (b) calculated LIF spectra of the $B\ ^2\Sigma_u^+$, v' = 0, N' $\leftarrow$ $X\ ^2\Sigma_g^+$, v" = 0, N" excitation of N_2^+ in the range 388.4 - 391.8 nm. The alternate structure of the rotational levels are clearly resolved. The intensities of the individual rotational lines can be calculated assuming Bolzmann distribution at rotational temperature of 300 K (see text). Each rotational line is convoluted with the sech^2 function of FWHM = 1.6 cm^{-1}.

Table 3-1. The rotational constants of N_2^+ and CO^+.

			v_0 /cm^{-1}	B_v	D_v
N_2^+	$X\,^2\Sigma_g^+$	v" = 0	25566.1	1.92235	6.10×10^{-6}
	$B\,^2\Sigma_u^+$	v' = 0		2.06873	6.17×10^{-6}
CO^+	$X^2\Sigma^+$	v" = 0	26345	1.96772	6.35×10^{-6}
	$A^2\Pi$	v' = 4		1.52143	6.6×10^{-6}

III-3.2. LIF spectrum of $CO^+(X\,^2\Sigma^+, v = 0)$

Figure 3-3 (a) shows the LIF spectrum of CO^+ in the range 378.9 - 382.0 nm. Excitation photon energy is 15.36 eV, which is equal to that of the *3d* (v = 2) Rydberg state converging to $CO^+(A\,^2\Pi)$ [9]. Fluorescence was dispersed by the monochromator at the wavelength of 451.88 nm corresponding to the transition $CO^+(A\,^2\Pi, v' = 4) \rightarrow CO^+(X\,^2\Sigma^+, v'' = 2)$. For getting a better signal-to-noise ratio, the GTI of Ti:sapphire was selected to the shorter pulse version.

The observed LIF spectrum is composed by overlapping the *P*, *Q* and *R* branches for the $CO^+(A\,^2\Pi, v' = 4) \leftarrow CO^+(X\,^2\Sigma^+, v'' = 0)$ transition as indicated in Fig. 3-3 (b). Individual rotational line in the LIF spectrum are convoluted with the $sech^2$ function of FWHM = 11 cm^{-1}. The rotational constants of $CO^+(A\,^2\Pi, v' = 4)$ and $CO^+(X\,^2\Sigma^+, v'' = 0)$ for the calculated spectrum are summarized in Table 3-1. The calculated spectrum at rotational temperature of 300 K is in good agreement with that of the observed one. That implies no remarkable change in the rotational state distribution as is denoted in the case of N_2.

The LIF signal count rate of $CO^+(X\,^2\Sigma^+, v'' = 0)$ at 379.6 nm, in which the maximum LIF intensity is observed, is approximately 200 times smaller than that of $N_2^+(X\,^2\Sigma_g^+, v'' = 0)$ reported in the previous section. That is simply because that the transition moment $CO^+(A\,^2\Pi, v' = 4) \leftarrow CO^+(X\,^2\Sigma^+, v'' = 0)$ is smaller than that for $N_2^+(B\,^2\Sigma_u^+, v' = 0, N') \leftarrow N_2^+(X\,^2\Sigma_g^+, v'' = 0, N'')$ in the same order as the observed one [5, 9].

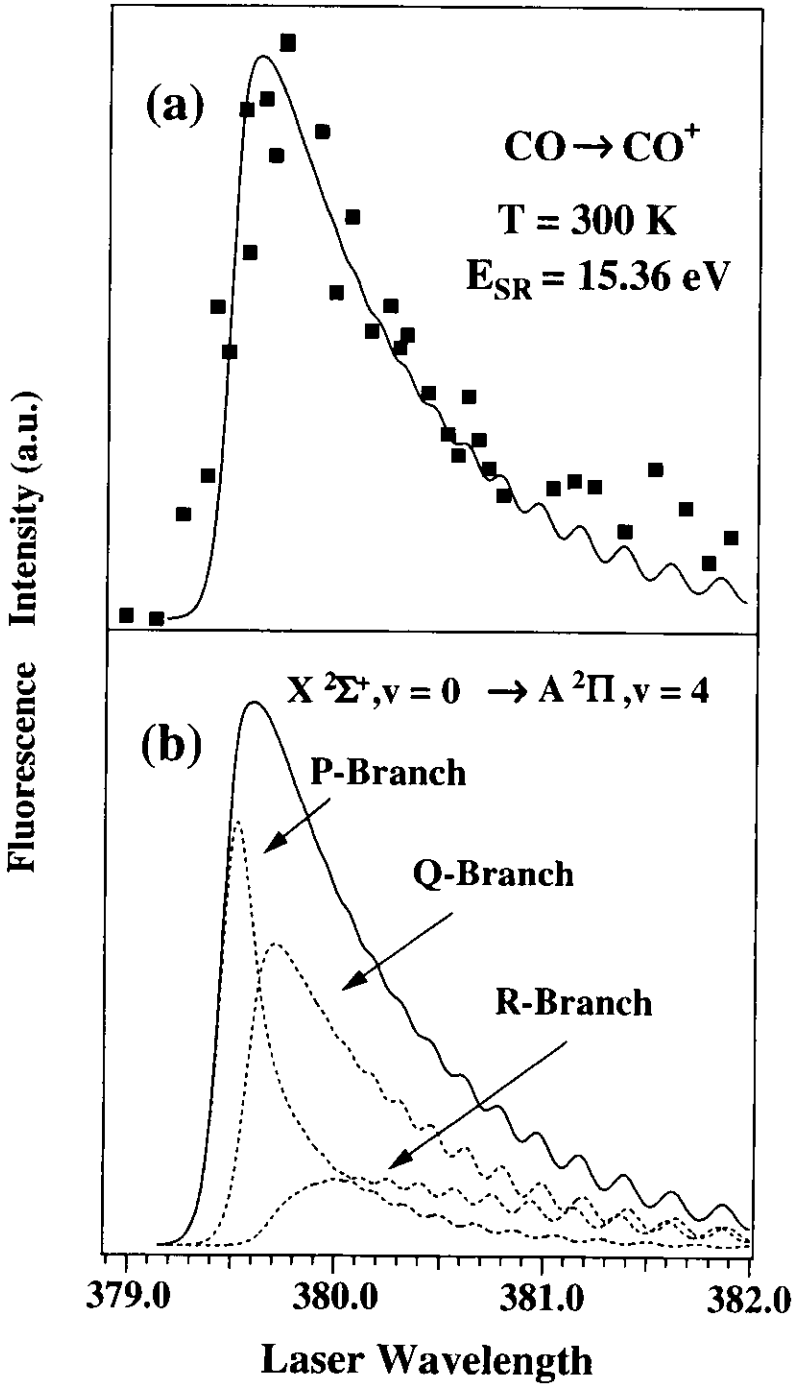

Figure 3-3. (a) Observed and (b) calculated LIF spectra of the CO^+ ($A\,^2\Pi$, v' = 4) ← CO^+ ($X\,^2\Sigma^+$, v'' = 0) excitation of CO^+ in the range 3278.9 - 382.0 nm. The excitation energies of undulator radiation are 15.36 eV which is consistent with the *3d* (v = 2) Rydberg state covering to CO^+ ($A\,^2\Pi$). The spectral resolution of the probe laser is 11 cm^{-1}. The spectrum (b) is composed by P, Q, R branches of individual rotational lines for $A\,^2\Pi$, -$X\,^2\Sigma^+$ transition of CO^+.

III-3.3. Yield curve of $N_2^+(X\,^2\Sigma_g^+, v = 0, 1)$ ionized from N_2.

We fixed the wavelength of the probe laser at the wavelength corresponds to the maximum LIF intensity in Fig. 3-4 (a), namely, 391.54 nm, and measured the LIF signal intensity as a function of E_{SR} in the range of 760 - 800 Å. Fluorescence was dispersed at the wavelength of 427.8 nm. To eliminate the second or higher order lights, an indium foil was inserted in the interrogating path of undulator radiation. For getting better signal-to-noise ratio, the GTI of Ti:sapphire laser was selected to the shorter pulse version. The spectral resolution of undulator radiation was 2 Å.

The observed spectrum shown in Fig. 3-4 (a) represents the yield curve for the v = 0 vibrational level of the $N_2^+(X\,^2\Sigma_g^+)$ ion. Peak structures are ascribed to the $nd\delta_g\ ^1\Pi_u$ or $nd\sigma_g\ ^1\Pi_u$ Rydberg series converging to the ionization threshold for $N_2^+(A\,^2\Pi)$ (I_E = 16.699 eV) [10] designated by tic marks in Fig. 3-4 (a). The $nd\delta_g\ ^3\Pi_u$ Rydberg series is discernible in a high-resolution photoionization spectrum [11], but is not denoted in Fig. 3-4 (a) owing to its small intensity. The present yield curve is in good agreement with the partial ionization cross section curve for $N_2^+(X\,^2\Sigma_g^+, v = 0)$ obtained by constant-ionic-state photoelectron spectroscopy [8, 12].

Next, the wavelength of the probe laser was set to 388.55 nm, which corresponds to the maximum position of the *P*-branch for the rotational structure of the transition $B\,^2\Sigma_u^+$, v' = 1 $\leftarrow X\,^2\Sigma_g^+$, v" = 1. Then, I measured the LIF intensity dependence on E_{SR} by scanning the undulator photon wavelength. The dispersed fluorescence was monitored at 423.6 nm, corresponding to the transition $B\,^2\Sigma_u^+$, v' = 1 $\rightarrow X\,^2\Sigma_g^+$, v" = 2, but fluorescence of the transition $B\,^2\Sigma_u^+$, v' = 0 $\rightarrow X\,^2\Sigma_g^+$, v" = 1 can not be completely eliminated due to the low resolving power of the monochromator. For this reason, the spectrum shown in Fig. 3-4 (b) was obtained by subtracting the intensity of the LIF signal at 391.54 nm (contributed purely by the v = 0 state) from that at 388.55 nm. The fluorescence intensity was normalized at 783 Å where only the $N_2^+(X\,^2\Sigma_g^+$, v"=0) state can be produced by photoexcitation.

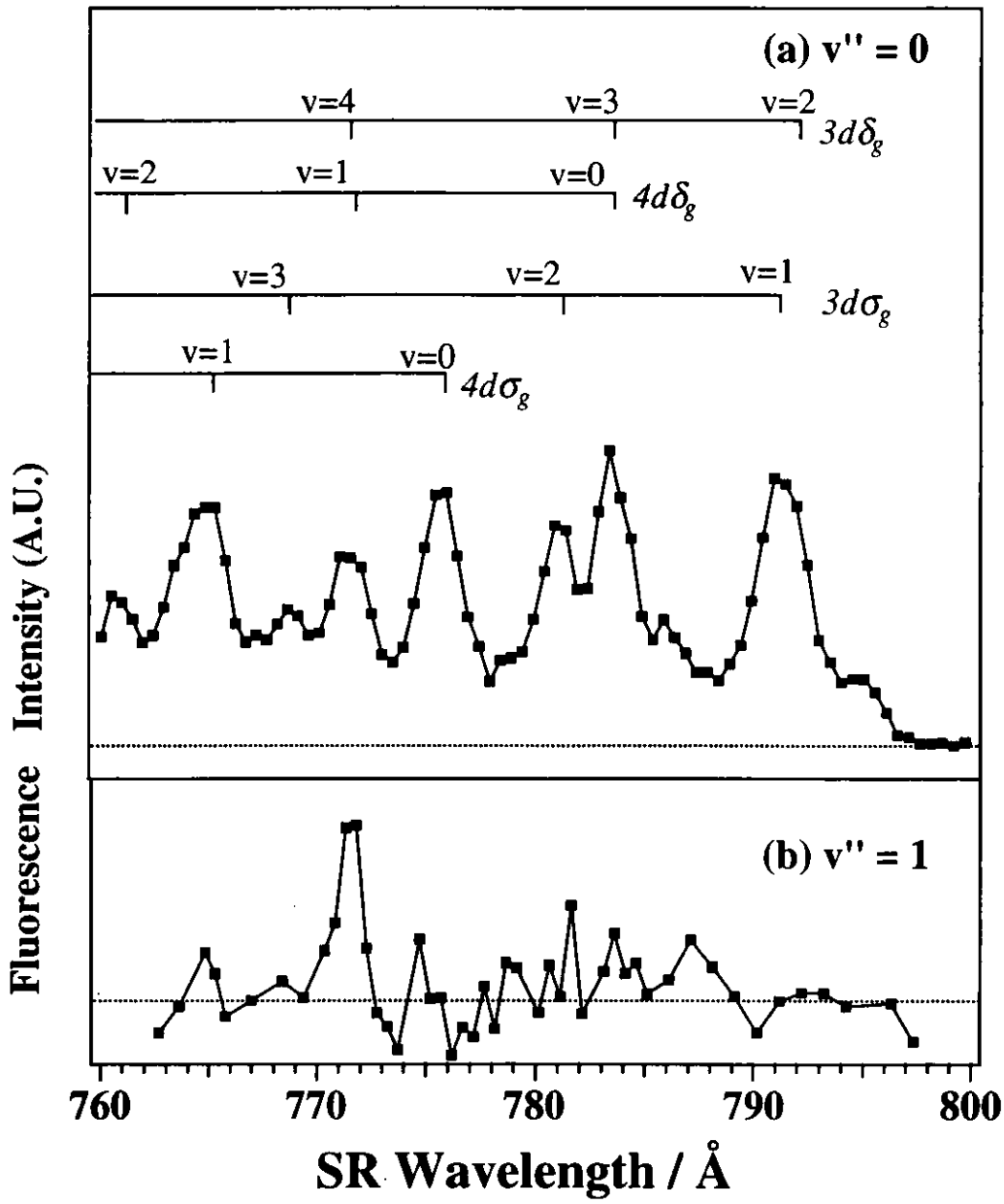

Figure 3-4. Yield curves for the vibrational levels of (a) v = 0 and (b) v = 1 of $N_2^+(X\ ^2\Sigma_g^+)$ in the range 760 - 800 Å. Several Rydberg series are indicated by tic marks. The spectral resolution of the undulator radiation was selected to be 2 Å.

The enhancement of the ionization yield for $N_2^+(X\ ^2\Sigma_g^+$, v = 1) is found at the peak of ~ 771.7 Å. This peak can be ascribed to the two Rydberg states, namely, $4d\delta_g$ (v = 1) (771.61 Å) and/or $3d\delta_g$ (v = 4) (771.5 Å) Rydberg states. On the other hands, the Rydberg states at 781.5Å (assigned to $3d\sigma_g$ [v = 2]) 775.8Å (assigned to $4d\sigma_g$ [v = 0]) and 764.9 Å (assigned to $4d\sigma_g$ [v = 1]) in the $N_2^+(X\ ^2\Sigma_g^+$, v = 0) yield curve cannot be recognized clearly in the $N_2^+(X\ ^2\Sigma_g^+$, v = 1) yield curve. The peak corresponds to 783.5 Å and 791.5 Å should not be observed because the ionization potential of $N_2^+(X\ ^2\Sigma_g^+$, v = 1) is located at 782 Å [11].

Holland *et a.l* reported that the vibrational branching ratios of $N_2^+(X\ ^2\Sigma_g^+$, v = 1) is ~ 0.9 at the Rydberg states of 771.6 Å, while the Rydberg states at around 775.8 Å and 764.5 Å are 0.1-0.2 by means of the constant-ionic-state photoelectron spectroscopy (CIS-PES). These results agree with those oberved in the present experiment, *i.e.*, the enhancement of the vibrational yeild at 771.6 Å. Now we have the reliable assignment of the Rydberg series converging to $N_2^+(A^2\Pi)$ state [10], a simple Franck-Condon analysis according to the deviation by Smith [11] and Eland [12] was performed here. Yield for $N_2^+(X\ ^2\Sigma_g^+$, v = 0 and v = 1) at a given Rydberg state is proportional to the vibrationally resolved ionization cross section, $\sigma_{i,v}$ [11]. Under the Born-Oppenhimer approximation for the electronic autoionization, *i.e.*, ignoring the *R*-dependence of the electrostatic coupling between a Rydberg state and the electronic continuum of $N_2^+(X\ ^2\Sigma_g^+)$, the values of $\sigma_{i,v}$ are given by [11]

$$\sigma_{i,v} \approx \sigma_i^{\max} \times \left|\left\langle \Lambda_{RYd} \middle| \Lambda_{v,ion} \right\rangle\right|^2 \equiv \sigma_v \qquad (3\text{-}3)$$

where $\left|\left\langle \Lambda_{RYd} \middle| \Lambda_{v,ion} \right\rangle\right|^2$ represents the Franck-Condon factor between Rydberg states and final vibrational states of ion, and $\sigma_i^{\max}$ the ionization cross section at the intensity maximum of the Rydberg state. Assuming the potential energy curves of Rydberg states converging to $N_2^+(A\ ^2\Pi)$ to be harmonic with the same equilibrium bond length and fundamental frequency as those of $N_2^+(A^2\Pi)$, Franck-Condon factors between vibrational states of Rydberg states and $N_2^+(X\ ^2\Sigma_g^+)$ can be replaced by those between $N_2^+(A\ ^2\Pi$, v) and $N_2^+(X\ ^2\Sigma_g^+$, v) [11].

The values of σ_v were calculated by Eq. (3-3) at Rydberg states of $4d\sigma_g$[v = 0] (775.8 Å), $3d\delta_g$, [v = 4] (771.5 Å), $4d\delta_g$ [v = 1] (771.6 Å), and $4d\sigma_g$ [v = 1] (764.5 Å), and summarized in Table 3-3. Franck-Condon factors between vibrational levels of N_2^+ ($X\ ^2\Sigma_g^+$, v") and N_2^+ ($A\ ^2\Pi_u$, v') are derived from those calculated in Ref. [5] and presented in Table 3-2. The values of σ_i^{max} were calculated by multiplying the absorption cross sections, σ_a, with the ionization efficiencies, γ. The calculation shows that σ_v = 6 at $3d\delta_g$ (v = 4) is larger than that of σ_v = 2 at $4d\delta_g$ (v = 1), leading the implication that the $3d\delta_g$, (v = 4) Rydberg state is responsible for the enhancement in the v = 1 curve of $N_2^+(X\ ^2\Sigma_g^+)$. However, the values for σ_v at $4d\sigma_g$ [v = 0] Rydberg state is larger than those of Rydberg states at 764.5 Å, 771.6 Å and 775.8Å, and the enhancement at 771.6 Å are not consistent with those obtained by this analysis. This may indicate that the potential energy curve of the Rydberg states is different from that of N_2^+ ($A\ ^2\Pi_u$, v'), resulting from the Rydberg- valence configuration interactions [14]. Further detailed analysis is necessary for the electronic autoionization process of Rydberg series converging to N_2^+ ($A\ ^2\Pi_u$, v') state, on the basis of the MQDT approach including the interaction of the electronic ionization continuum and the Rydberg states.

Table 3-2. Franck-Condon factors between $N_2^+(X\,^2\Sigma_g^+, v)$ and $N_2^+(A\,^2\Pi, v)$ [5].

$X^2\Sigma_g^+$ \ $A^2\Pi$	v' = 0	v' = 1	v' = 3	v' = 4
v" = 0	0.4974	0.3190	0.1265	0.01128
v" = 1	0.3718	0.04404	0.2364	0.09623

Table 3-3. Summary of the estimated value and assignment of Rydberg states.

Wavelength / Å	Assignment	σ_a [#1]	γ [#2]	σ_i	σ_v	
					v" = 0	v" = 1
775.8	$4d\sigma_g$ [v = 0]	180	0.6	108	28	40
771.5	$3d\delta_g$ [v = 4]	80	0.70	56	0.6	50
771.6	$4d\delta_g$ [v = 1]	130	0.40	52	17	1.6
764.5	$4d\sigma_g$ [v = 1]	140	0.65	91	29	2.7

[#1] σ_i [10^{18} cm^2] is the absorption cross section directly read from Fig. 1 reported in Ref. [13].

[#2] γ is the ionization efficiency directly read from Fig. 1 reported in Ref. [13].

III-3.4. Rotational State Distribution of $N_2^+(X\ ^2\Sigma_g^+,\ v = 0)$ from N_2O.

Figure 3-5 shows the (a) N_2O^+ and (b) N_2^+ ion yield curves in the range 615 - 715 Å measured by the time-of-flight mass spectrometry. The peak structure in the yield curve is identified as the $nd\pi$ and $nd\sigma$ Rydberg series converging to the ionization potential of $N_2O^+ C\ ^2\Sigma^+$ state ($I_E = 20.105$ eV) [15-19]. The molecular orbital configuration of N_2O in its electronically ground state is

$$(1\sigma)^2(2\sigma)^2(3\sigma)^2(4\sigma)^2(5\sigma)^2(6\sigma)^2(1\pi)^4(7\sigma)^2(2\pi)^4 \quad {}^1\Sigma^+. \qquad (3\text{-}4)$$

An excitation of electron from 6σ orbital to the Rydberg orbital leads to the excited states with several electronic configurations. Although only two Rydberg series are identified in the present yield curve, the five Rydberg series whose electronic configurations can be identified to $ns\sigma$, $np\sigma$, $np\pi$, $nd\sigma$, and $nd\pi$ have been observed in the high resolution mass spectrometry with 0.8 Å spectral resolution [20]. While the intensities of the $nd\sigma$, and $nd\pi$ Rydberg series are comparable with those in N_2O^+ yield curve, the intensities of the $nd\sigma$ Rydberg series in the N_2^+ yield curve is smaller than those for the $nd\pi$ Rydberg series. This implies that the yield of the N_2O^+ and N_2^+ depend on the types of Rydberg series, which have been discussed in detail by Berkowitz *et al* [17]. The arrow in the yield curve of N_2^+ at 725 Å indicates thermochemical dissociation limit for $N_2^+(X\ ^2\Sigma_g^+) + O(^3P)$. Table 3-4 summarizes both the dissociation limits of fragments and the ionization thresholds of N_2O^+.

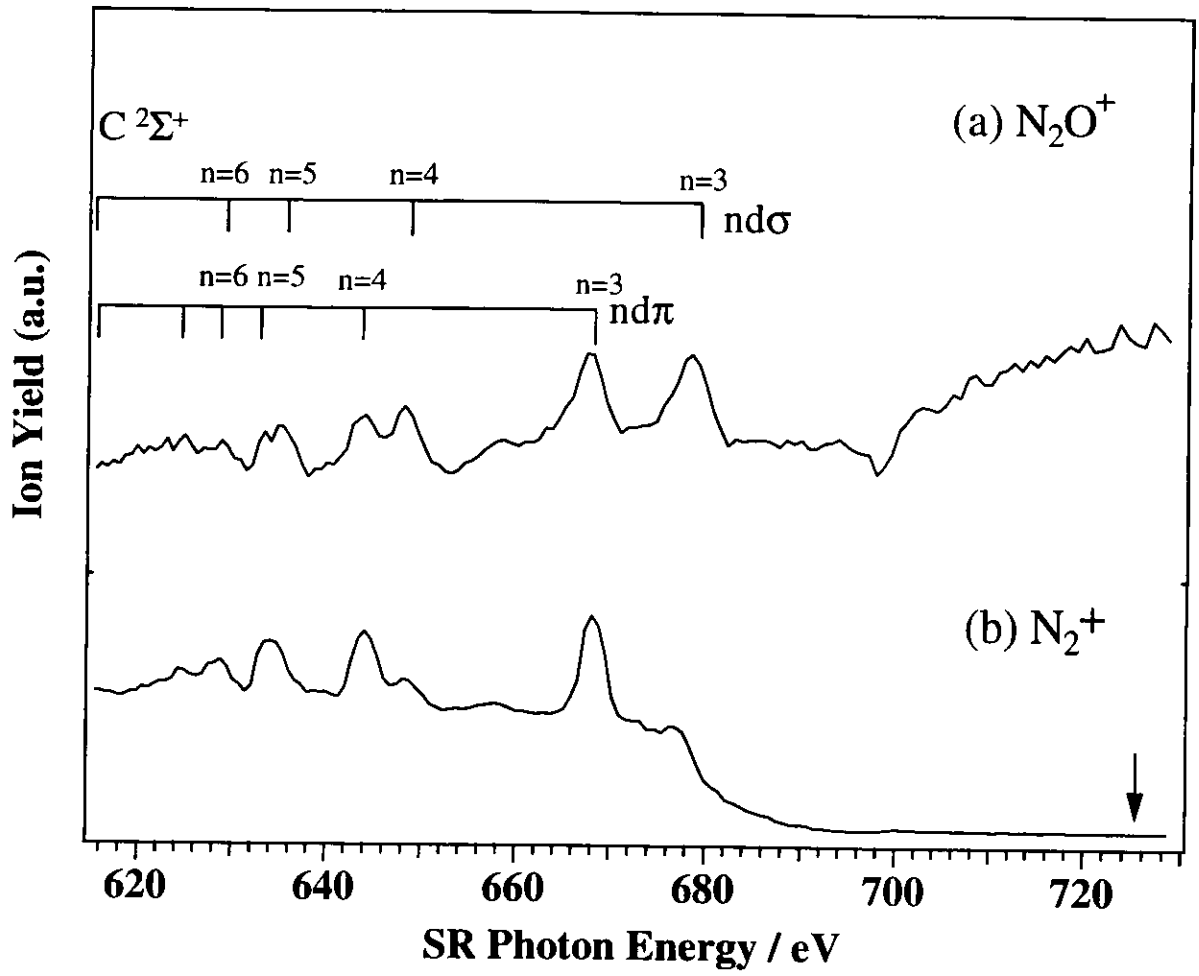

Figure 3-5. Yield curve for N_2O^+ and N_2^+ produced by undulator radiation excitation of N_2O in the range 615 - 730 Å. The spectral resolution is 2.4 Å. The structure in the yield curves are identified with the *ndσ* and *ndπ* Rydberg series converging to N_2O^+ ($C^2\Sigma^+$). The arrow in the N_2^+ yield curve indicates the thermochemical dissociation limit for $N_2^+(X\,^2\Sigma_g^+, v = 0) + O(^3P)$.

Table 3-4. Adiabatic ionization potentials and Disscoiation limit of N_2O.

Key[#1]	Energy / eV[#2]	Species	Symmetry
I_p	12.89	$N_2O^+\left[X^2\Pi(0,0,0)\right]$	$^2\Pi$
I_p	16.38	$N_2O^+\left[A^2\Sigma^+(0,0,0)\right]$	$^2\Sigma$
D	17.25	$N_2^+(X^2\Sigma_g^+)+O(^3P_g)$	$^{2,4}\Sigma^-$, $^{2,4}\Pi$
I_p	18.2[#3]	$N_2O^+\left[B^2\Pi(0,0,0)\right]$	$^2\Pi$
D	18.37	$N_2^+(A^2\Pi_u)+O(^3P_g)$	$^{2,4}\Pi$, $^{2,4}\Delta$, $^{2,4}\Sigma^+$, $^{2,4}\Sigma^-$
D	19.22	$N_2^+(^2\Sigma_g^+)+O(^1D_g)$	$^2\Sigma^+$, $^2\Pi$, $^2\Delta$
D	20.34	$N_2^+(A^2\Pi_u)+O(^1D_g)$	$^2\Sigma^+$, $^2\Sigma^-$, $2(^2\Pi)$, $^2\Delta$, $^2\Phi$
D	20.42	$N_2^+(B^2\Sigma_u)+O(^3P_g)$	$^2\Sigma^-$, $^2\Pi$
I_p	20.11	$N_2O^+\left[C^2\Sigma^+(0,0,0)\right]$	$^2\Sigma$

[#1] The symbols I_p and D refer to the adiabatic ionization potential and the limit for dissociation.

[#2] All energies are measured with respect to the neutral ground state $N_2O\left[X^1\Pi(0,0,0)\right]$.

[#3] This is the energy at most intense peak observed in photoelectron spectrum.

Figure 3-6 (a) shows an LIF spectrum of N_2^+ produced from N_2O at E_{SR} = 18.556 eV. This agrees with the excitation energy of $3d\pi$ Rydberg state converging to $N_2O^+(C^2\Sigma)$. The shorter pulse of the second harmonic of the probe laser was used to get a larger power. Two maxima centered at 391.54 nm and 390.8 nm are ascribed to the *P* and *R* branches, respectively, of $N_2^+(B^2\Sigma_u^+, v' = 0, N') \leftarrow N_2^+(X^2\Sigma_g^+, v'' = 0, N'')$. The rotational temperature of N_2^+ in Fig. 3-6 (a) is estimated to be 200 - 230 K by fitting observed data points. The solid line represents the calculated curve at T = 220 K. The observed spectrum is slightly shifted to the red side with respect to the calculated spectrum. For comparison, an LIF spectrum of N_2^+ produced from N_2 is shown in Fig. 3-6 (b) which is taken with the same resolution of the laser. The spectrum in Fig. 3-6 (b) is in good agreement with the calculated curve (solid line) at T = 300 K convoluted with a resolution of 11 cm^{-1}.

Dissociation leading to $N_2^+(X^2\Sigma_g^+) + O(^3P)$ is known to be promoted at E_{SR} = 18.556 eV by autoionization of the $3d\pi$ Rydberg state to the $N_2O^+(B^2\Pi)$ state [17]. In general, change in the rotational distribution during autoionization is insignificant as is discussed in Sec. III-3.1, so that the rotational temperature of $N_2O^+(B^2\Pi)$ is almost equal to that of the parent N_2O molecule, *i.e.*, 300 K. Thus, a conclusion derived from Fig. 3-6 (a) is that the rotational temperature of N_2^+ ($X^2\Sigma_g^+$, v = 0) is substantially reduced in the course of the dissociation. It is evident that the mechanism for the dissociation of $N_2O^+(B^2\Pi)$ is not direct dissociation but predissociation [15], because vibrational progressions of the $B^2\Pi$ state are found in the range 17.65 - 19.0 eV in a photoelectron spectrum of N_2O [20]. The energy released at a time of dissociation, referred to here as the *available* energy E_{avl}, is defined by [21]

$$E_{avl} = E_{SR} - E_{elec} - D_0 = I_E - D_0 \qquad (3\text{-}5)$$

where E_{SR} is the excitation photon energy for the $3d\pi$ Rydberg state (E_{SR} = 18.556 eV), D_0 is the NN-O bond dissociation energy (17.25 eV measured from the electronically ground state of N_2O), E_{elec} is the kinetic energy of the ejected electron, and I_E is the ionization energy for a

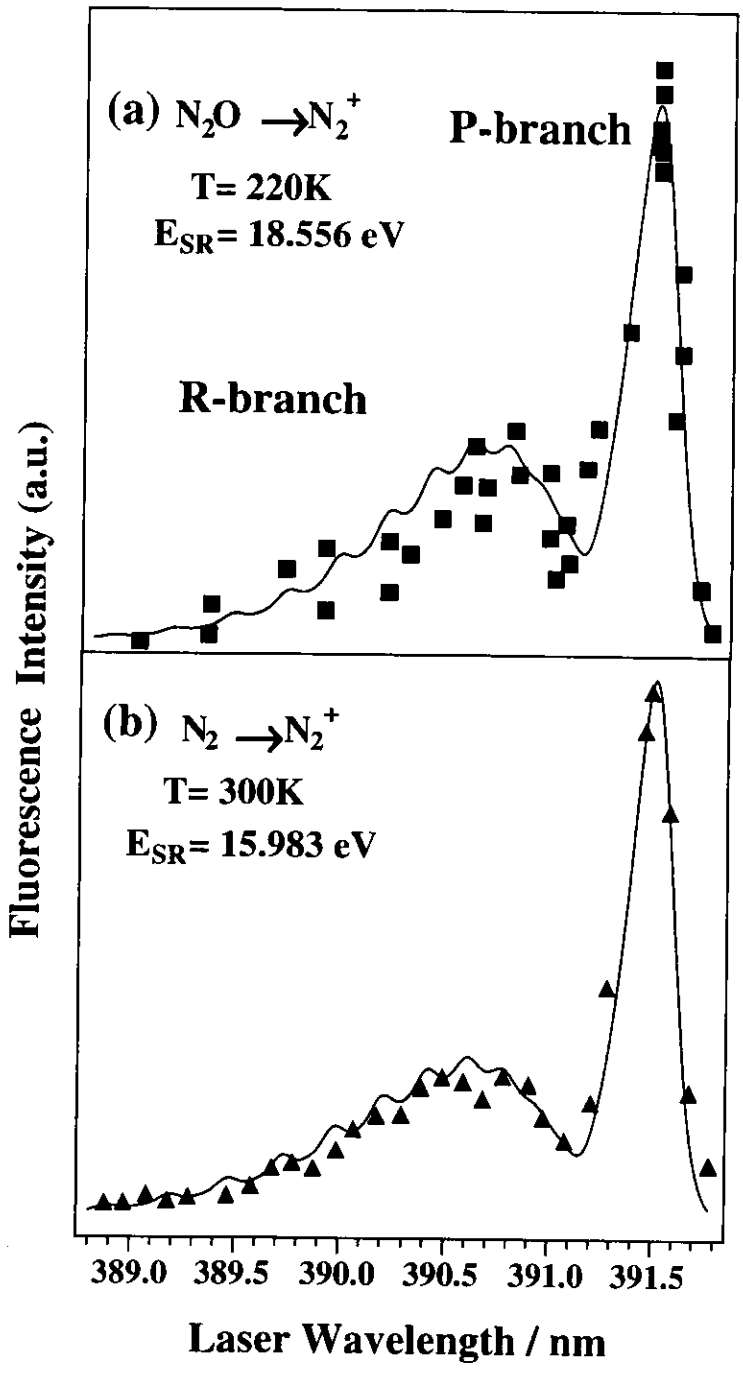

Figure 3-6. LIF spectra of the $B\ ^2\Sigma_u^+$, v' = 0, N' $\leftarrow$ $X\ ^2\Sigma_g^+$, v" = 0, N" excitation of N_2^+ produced from (a) N_2O and (b) N_2. The excitation energies of undulator radiation are 18.556 and 15.983 eV, respectively. The spectral resolution of the probe laser is 11 cm^{-1}. The solid lines represent the calculated curves with the rotational temperature of (a) 220 and (b) 300 K.

vibrational state of N_2O^+ ($B\ ^2\Pi$) [20]. The available energy and the initial rotational energy of $N_2O^+(B\ ^2\Pi)$ can be distributed among the vibrational and rotational energy of $N_2^+(X\ ^2\Sigma_g^+)$.

The available energy is calculated from an Eq. (3-5) to be 3200 - 10500 cm^{-1} depending on I_E. On the other hand, the average rotational energy of the N_2^+ ($X\ ^2\Sigma_g^+$, v = 0) fragment is obtained from T = 220 K to be 150 cm^{-1}. The percentage of the rotational energy of $N_2^+(X\ ^2\Sigma_g^+$, v = 0) to the available energy is thus only 1.5 - 5 %. This small fraction of the fragment rotational energy indicates that the available energy is distributed dominantly to the relative translational energies of N_2^+ and O and/or to the fragment vibrational energy.

A lot of theoretical treatments have been proposed for analyzing the internal state distributions of fragments produced by photodissociation: phase space theory [22-24], analysis basen on the adiabatic channel model [25-27] and the impulsive model [28-30], the semiclassical analysis [31], and the full quantum mechanical analyis [32-36] with model or *ab initio* potential energy surfaces. Phase space theory is a simple statistical theory based on the assumption that all final states can be populated with a equal probability, *i.e.*, the probability for finding a final state in a specified eigenphase is proportional to the number of ways that the available energy can be distributed under the constrain of the angular momentum and the total energy conservation. For the present case, the probability for populating the rotational level j of $N_2^+(X\ ^2\Sigma_g^+$, v = 0) is given by

$$N(j, E_{avl}) = (2j+1)\sum_J \sum_{\ell=0}^{\ell_{max}} \ell, \qquad (3\text{-}6)$$

where ℓ represents the angular momentum of relative motion between N_2^+ and O, ℓ_{max} represents the maximum value for ℓ, J represents the angular momentum of the initial N_2O^+ ($B\ ^2\Pi$). The value for ℓ is taken in the range

$$|J - j| < \ell < |J + j| \qquad (3\text{-}7)$$

by the constrain of angular momentum conservation. Assuming the long-range ion-moleculer

induced dipole interaction and ignoring the repulsive part of the short-range electronic potential, the *effective* potential energy is given by

$$V_{eff} = -\frac{\alpha e^2}{2(4\pi\varepsilon_0)^2}\frac{1}{r^4} + \frac{l(l+1)\hbar^2}{2\mu r^2} \qquad (3\text{-}8)$$

where α represents the polarizability, ε_0 represents the permittivity of free space, e represents the electron charge, and μ represents the reduced mass between N_2 and O. In order to dissociate, the following condition should be satisfied

$$E_{tr} = E_{avl} - E_{rot} - E_{vib} \geq V_{eff}. \qquad (3\text{-}9)$$

The value for ℓ_{max} can thus be given from Eq. (3-8) and Eq. (3-9)

$$l_{\max} = \frac{1}{2}\sqrt{16\frac{C^{1/2}\mu E_{tr}^{1/2}}{\hbar^2} + 1} - \frac{1}{2}$$
$$C = \frac{\alpha e^2}{2(4\pi\varepsilon_0)^2} \qquad (3\text{-}10)$$

where μ represents the reduced mass, and $\hbar$ is the Plank's constant. Figure 3-7 shows the LIF spectrum (direct line) calculated using the rotational state distribution estimated by Eq. (3-6) and Eq. (3-10), as well as the observed data (black square) and the spectrum calculated using a Boltzmann distribution with a rotational temperature of 230 K (dashed line). The value for C is calculated to be 1×10^{-58} [J m^4] by assuming the value of α to be 10^{-30} [m^3]. The population of the initial rotational state, J, of N_2O^+ is assumed to be prepared by a Bolzmann distribution at 300 K. The large difference in the observed data with the calculated spectrum indicates that the phase space theory is not adequate for accounting the reduction of the rotational temperature for dissociation of $N_2O^+(B\ ^2\Pi)$. This implies also the initial rotational state of N_2O^+ $(B\ ^2\Pi)$ may be coupled with a particular final rotational state of fragment instead of distributing all final state equally. Adiabatic channel model [25-27] can also provide the value for ℓ_{max} by constructing the model potential which correlates adiabatically the internal states of the initial states and final fragment, but this is not treated furthermore in the present study.

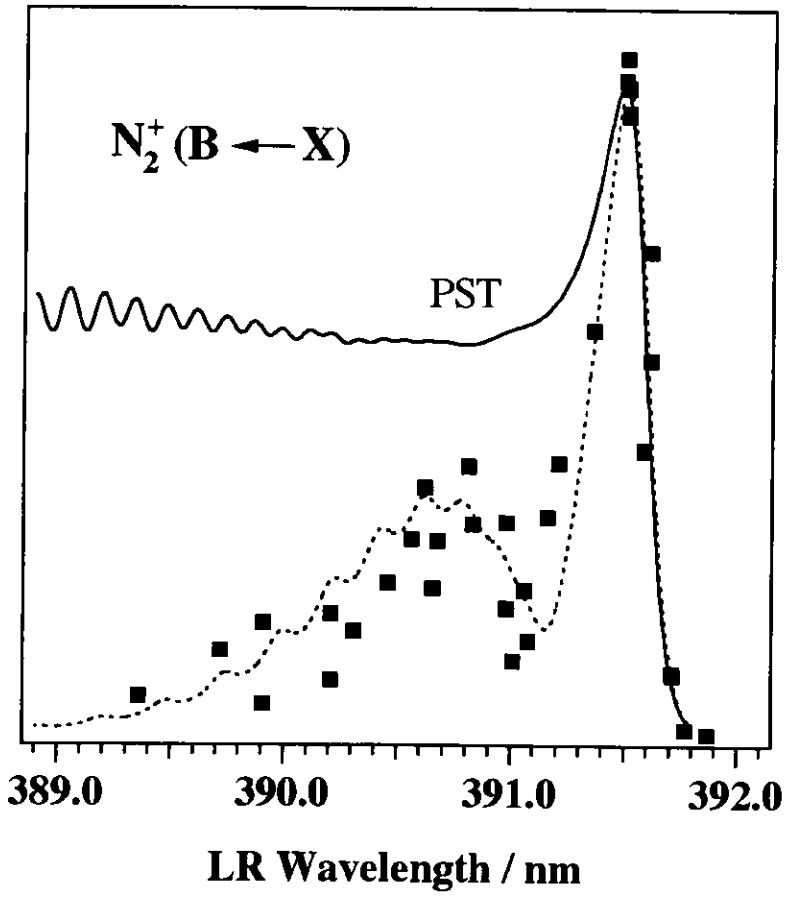

Figure 3-7. LIF spectrum of $B\ ^2\Sigma_u^+$, v' = 0, N' ← $X\ ^2\Sigma_g^+$, v" = 0, N" excitation of N_2^+ calculated by phase space theory (solid line) as well as by Boltzmann distribution of 230 K (dotted line). The available energy is 3200 cm^{-1}. Black squares represents the observed data.

While the phase space theory assumes the energy randomization during dissociation, the impulsive model [28] assumes that the molecules dissociate so rapid that the available energy can not be randomized to the all phase space equally but is specified by the geometry at a instance of dissociation. Under the assumption of the impulsive model, the repulsive force are applied to the NN bond suddenly, and its component perpendiculat to NO bond is responsible for the rotational energy distribution [28]. Under this assumption, the distribution of E_{avl} to the fragment rotational and/or vibrational energy of fragments are evaluated by using E_{avl}, the masses of the three atoms and the bond angle, θ ,of $N_2O^+(B\ ^2\Pi)$ in its equilibrium geometry. Unfortunately, the exact equilibrium geometry of N_2O^+ $(B\ ^2\Pi)$ has not been elucidated yet because of a strong vibronic coupling between two electronic states located at around 17.5 eV whose configurations are expressed as $(2\pi)^{-2}$ $(3\pi)^1$ and $(1\pi)^{-1}$ [37]. It is possible that the ion with the former configuration has a bent equilibrium geometry on account of the accommodation of an electron in the π^* orbital [38]. Furthermore, the vibrational state distribution of $N_2^+(X\ ^2\Sigma_g^+)$ can not be measured owing to the limited wavelength coverage of our Ti:sapphire laser. Therefore, I calculate the average rotational energy of $N_2^+(X\ ^2\Sigma_g^+$, v = 0) classically as a function of θ by a similar procedure to that reported by *Levine* and *Valentini* [39] who have assumed a *stiff* NN bond and no vibrational excitation (*modified* impulsive model [28]). For simplicity, I make further assumptions: The bond length of NN-O is equal to that of N-NO, the three atoms have the same mass, and the dissociation is assumed to proceed on the plane where the three atoms are located. The contribution of the bending motion to the fragment rotational energy is disregarded. A space-fixed Cartesian coordinate system is employed with the origin at the center of mass of N_2O^+. The rotational angular momentum of $N_2O^+(B\ ^2\Pi)$ perpendicular to the molecular plane, namely, J_C, is taken as the initial angular momentum even in the C_s bent geometry.

The procedure of the calculation is briefly described as follows. The angular momentum applied to each atom resulting from the initial rotation of $N_2O^+(B\ ^2\Pi)$ is calculated by the distance from the center of mass to each atom and the *average* angular velocity at a room

temperature. The angular momentum resulting from the repulsive force is estimated and related to the E_{avl} by using the conservation law of the linear momentum. Explicit forms of the angular momenta of relative motion of the fragments O and N_2^+ and the rotational angular momentum of N_2^+ are substituted into the equation of the conservation law of the angular momentum and the final rotational energy of the fragment is obtained. The details are presented in Appendix III-A.

Figure 3-8 shows the calculated rotational energy of $N_2^+(X\ ^2\Sigma_g^+, v = 0)$ as a function of θ when E_{avl} takes a value of 3200 cm^{-1}, assuming that the dissociation takes place from the vibrational ground state of $N_2O^+(B\ ^2\Pi)$, *i.e.*, at the lowest peak of the vibrational band (I_E = 17.65 eV) in the reported photoelectron spectrum [20]. Two rotational energies were calculated which correspond to two extreme cases [40]: the high J limit and low J limit. Those are classified by the direction between the initial rotation of $N_2O^+(B\ ^2\Pi)$ and the repulsive force generated at a time of dissociation (see appendix III-A). In the low J limit the calculated curve once goes down to zero and goes up again with decreasing bond angle. The increase in the rotational energy with decreasing bond angle is attributed to the increase in the component of the rotational angular momentum of $N_2^+(X\ ^2\Sigma_g^+, v = 0)$ resulting from the repulsive force. The dashed line at the rotational energy of 200 cm^{-1} shows the initial rotational energy of $N_2O^+(B\ ^2\Pi)$ at 300 K. The rotational energy of $N_2^+(X\ ^2\Sigma_g^+, v = 0)$ is smaller than that of the parent $N_2O^+(B\ ^2\Pi)$ at $\theta \geq 130°$ and $\theta \geq 165°$ in the low-J and high-J limits, respectively. This clearly suggests the possibility of less rotational excitation in $N_2^+(X\ ^2\Sigma_g^+, v = 0)$ than in $N_2O^+(B\ ^2\Pi)$ at $\theta \geq 130°$. The LIF spectrum of $N_2^+(X\ ^2\Sigma_g^+, v = 0)$ has demonstrated that the average rotational energy of $N_2^+(X\ ^2\Sigma_g^+, v = 0)$ is smaller than that of $N_2O^+(B\ ^2\Pi)$. From these considerations, we can draw the conclusion that the equilibrium bond angle for the vibrational ground state of $N_2O^+(B\ ^2\Pi)$ is larger than ~ 130°.

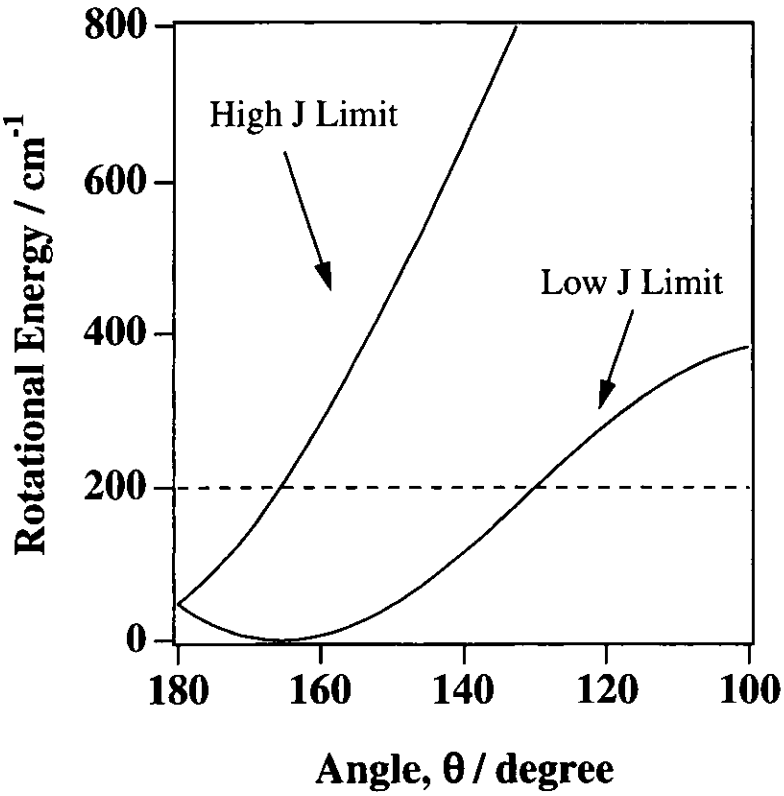

Figure 3-8. Calculated rotational energies of the N_2^+ fragment as a function of the bond angle θ on the basis of the modified impulsive model. Two rotational energies were calculated which correspond to the high J and low J limit (see text). The dashed line at the rotational energy of 200 cm^{-1} shows the initial rotational energy of N_2O^+ at 300 K.

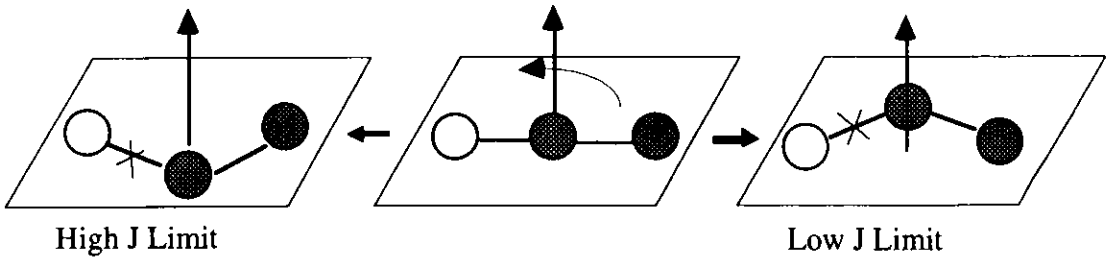

Figure 3-9. Schematic diagram of high J limit and low J limit configuration. They are prepared by bending to the different direction from linear configuration of the Rydberg states or neutral ground states. The arrows indicates schematically the direction of the angular momentum of initial motion. The shaded circle in the figure indicates N atom.

We can illustrate the picture for the process: the geometry of $N_2O^+(B^2\Pi)$ prepared by autoionization or direct ionization process starts to bent from a linear geometry and then the dissociation occurs after several periods of vibrational motion. The $3d\pi$ Rydberg state converging to the $N_2O^+(C^2\Sigma^+)$ state and the $N_2O(X\ ^1\Sigma^+)$ electronic ground state have reported to be a linear geometry [20]. The configuration leading to the high J and low J limit can be thus prepared by bending from linear configuration to the different direction as is shown in Fig. 3-9 schematically. In both cases, the effect of the bending motion on the rotational state distribution of fragments should be included in the calculation, and bending motion leads to the increase of the rotational energy of the fragment. Hence, the bond angle for $N_2O^+(B\ ^2\Pi)$ would be actually larger than that estimated according to the modified impulsive model.

Thermalization effect on diturbing the fragment rotational state distribution in the ion trap cell is considered to be small or negligible. It can be confirmed from the fact that the rotational state distribution of N_2^+ ($X\ ^2\Sigma_g^+$, v = 0) depends on the excitation energy of the undulator radiation. LIF spectra are shown in Fig.3-10 for the excitation energy of E_{SR} = 28.5 eV, 33 eV, 21 eV as well as 18.556 eV. The rotational temperatures of N_2^+ ($X\ ^2\Sigma_g^+$, v = 0) are determined to be 550 K at E_{SR} = 28.5 and 33 eV. In the spectra at 21 eV, the temperature is found to be lower than 300 K though the rotational state distribution seems not to obey the Bolzmann distribution. The further details on the rotational state distributions of N_2^+ at these photon energies will be expected, but it is not treated in the present paper because it seems that multiple dissociation paths leading to $N_2(X\ ^2\Sigma_g^+$, v = 0) make the analysis much more difficult.

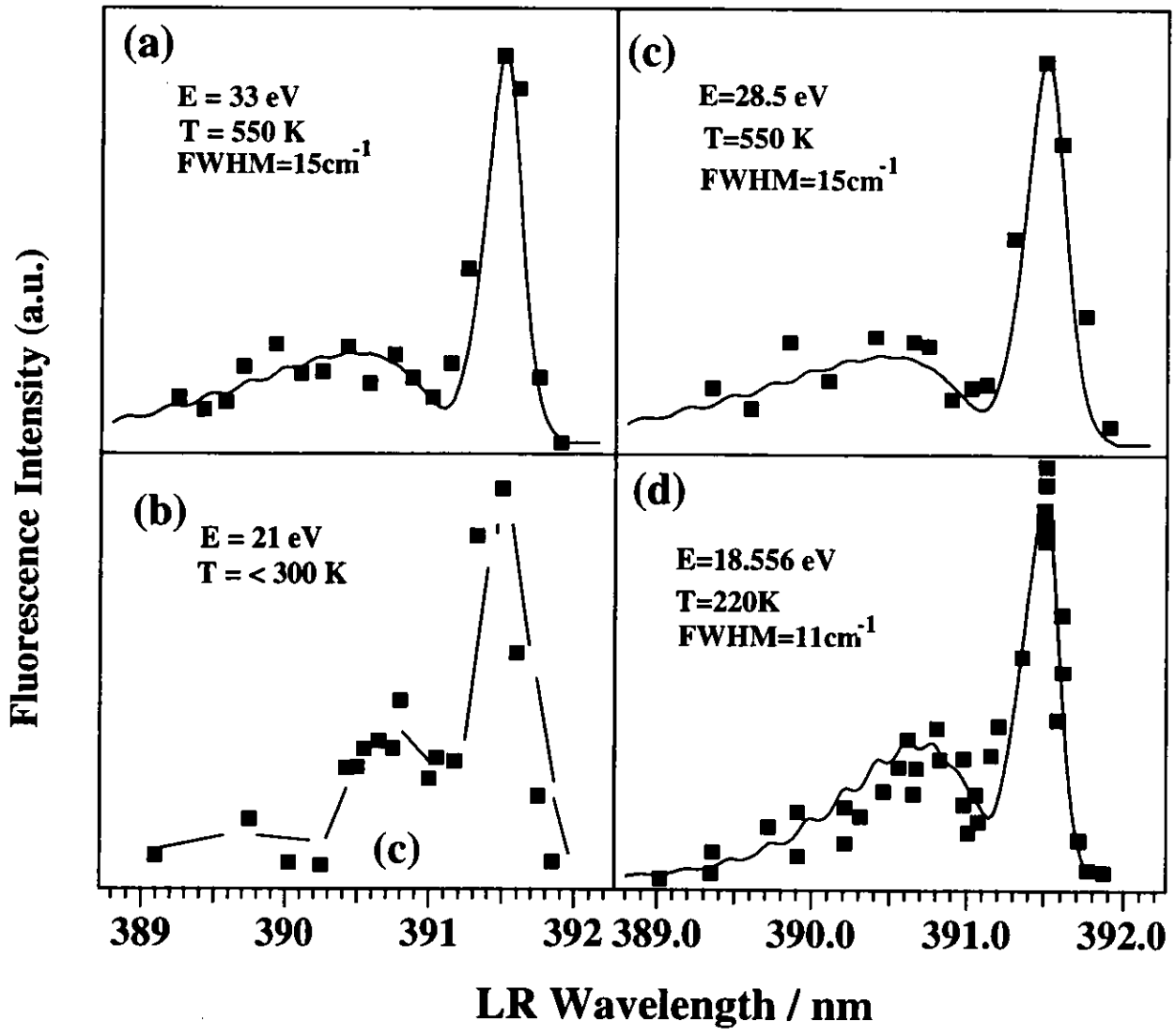

Figure 3-10. LIF spectra of $N_2^+(B\ ^2\Sigma_u^+, v' = 0) \leftarrow N_2^+(X\ ^2\Sigma_g^+, v'' = 0)$ produced by the undulator radiation excitation of N_2O at (a) 33 eV, (b) 28.5 eV, (c) 21 eV and (d) 18.556 eV. While the rotational temperature of (d) is estimated to 220 K, those of (a) and (b) are estimated to 550 K. The excitation photon energy of the rotational temperature of fragment implies that thermalization of the rotational state distribution is negligible or small.

IV Conclusion

Pump-probe spectroscopy combined with laser and synchrotron radiation is performed for the ionization and dissociation dynamics of N_2 and N_2O in the extreme ultraviolet energy region. The N_2^+ ($X\ ^2\Sigma_g^+$, v, N) ion produced from N_2 or N_2O with synchrotron radiation excitation is detected by laser induced fluorescence (LIF) spectroscopy. To increase the number density of ions produced by photoexcitation of synchrotron radiation, a cylindrical ion trap cell is employed. The effect of thermalization on the internal state distributions of N_2^+ ion can be ignored in the ion trap. The rotational structures of the electronic excitation $B\ ^2\Sigma_u$, v' = 0, N' ← $X\ ^2\Sigma_g^+$, v" = 0, N" of N_2^+ produced from N_2 are clearly resolved by using a narrow band width of Ti:sapphire laser. The LIF spectrum of $CO^+(X\ ^2\Sigma^+$, v = 0) produced by undulator radiation excitation of CO is also measured by LIF spectroscopy. The yield curves for N_2^+ ($X\ ^2\Sigma_g^+$, v = 0, 1) are also measured as a function of the photon energy of synchrotron radiation. The rotational temperature of $N_2^+(X\ ^2\Sigma_g^+$, v = 0) produced from $N_2O^+(B\ ^2\Pi)$ was determined from an LIF spectrum to be in the range 200-230 K. This indicates the rotational temperature of N_2^+ ($X\ ^2\Sigma_g^+$, v = 0) is substantially reduced in the course of the dissociation. The modified *impulsive model* well accounts for the reduction of the rotational temperature. This implies that the initial energy of N_2O^+ may not be distributed among the all final state statistically equally but some specific internal states of fragments, which are related to the geometry of the $N_2O^+(B^2\Pi)$ states. The analysis based on the *impulsive model* indicates that the equilibrium bond angle of the vibrational ground state of $N_2O^+(B\ ^2\Pi)$ is larger than 130°.

Appendix III-A

This appendix shows the method for calculating the fragment rotational energy as a function of the molecular bond angle, θ. First, we set the coordinates of three atoms, denoted *A*, *B*, *C* in a space-fixed Cartesian coordinatet as shown in Figure III-A-1. The center of mass is always taken to the origin of this coordinate system. The position of *B* is always on the *y* axis and the bond length, *r*, is kept to be constant. The angles α and φ are defined as denoted in the figure. The Cartesian coordinates of *A* (xa, ya), *B* (xb, yb), and *C* (xc, yc) are given using *r* and θ by

$$\begin{aligned} xc^2 &= \tfrac{1}{4}\left(r^2\left[-2\cos\{\theta\}+2\right]\right) \\ yc^2 &= \tfrac{1}{18} r^2\left(\cos[\theta]+1\right) \\ yb^2 &= \tfrac{2}{9} r^2\left(\cos[\theta]+1\right) \end{aligned} \qquad \text{(3-A-1)}$$

and

$$\begin{aligned} ya &= yc \\ xa &= -xc \\ xb &= 0 \end{aligned}$$

respectively. The coordinates of the center of mass of diatomic molecules, BC, are given using *r* and θ by

$$\begin{aligned} xbc^2 &= \tfrac{1}{8} r^2\left(-\cos[\theta]+1\right) \\ ybc^2 &= \tfrac{1}{72} r^2\left(\cos[\theta]+1\right). \end{aligned} \qquad \text{(3-A-2)}$$

The distance of each atom from the center of mass, namely, *ra*, *rb* and *rc* is given using *r* and θ by

$$\begin{aligned} ra^2 &= r^2\left(\tfrac{1}{9}\left[-4\cos\{\theta\}+5\right]\right) \\ rb^2 &= \tfrac{2}{9} r^2\left(\cos[\theta]+1\right) \\ rc^2 &= r^2\left(\tfrac{1}{9}\left[-4\cos\{\theta\}+5\right]\right). \end{aligned} \qquad \text{(3-A-3)}$$

The relation of the angle α and θ are given by

$$\sin(\alpha) = \tfrac{1}{2}\frac{\sqrt{2}\sqrt{\cos(\theta)+1}}{\sqrt{-4\cos(\theta)+5}},\ \cos(\alpha) = \sqrt{-\tfrac{1}{2}\frac{\cos(\theta)+1}{-4\cos(\theta)+5}+1}\ . \qquad \text{(3-A-4)}$$

The relation of the angle φ and θ are given by

$$\varphi = \frac{\pi - \theta}{2}. \tag{3-A-5}$$

The low J and high J limit are classfied by the corration of the direction between the initial rotational motion and the repulsive force generated at a time of dissociation as is shown in the Figure III-A-2.

The linear momentum conservation in terms of A atom and BC diatomic molecule during dissociation leads to the following equations for low J and high J limit.

For low J limit

$$\begin{aligned} m\ \mathrm{Vax} &= m\ \mathrm{ra}\, w\ \sin(\alpha) - \mathrm{FT}\cos(\varphi) \\ m\ \mathrm{Vay} &= -m\ w\ \mathrm{ra}\cos(\alpha) - \mathrm{FT}\sin(\varphi) \end{aligned} \tag{3-A-6}$$

$$\begin{aligned} 2m\ \mathrm{Vbcx} &= \mathrm{FT}\cos(\varphi) + m\ \mathrm{rc}\, w\ \sin(\alpha) - m\ w\ \mathrm{rb} \\ 2m\ \mathrm{Vbcy} &= m\ w\ \mathrm{rc}\cos(\alpha) + \mathrm{FT}\sin(\varphi) \end{aligned} \tag{3-A-7}$$

For high J Limit

$$\begin{aligned} m\ \mathrm{Vax} &= -\mathrm{FT}\cos(\varphi) - m\ w\ \mathrm{ra}\sin(\alpha) \\ m\ \mathrm{Vay} &= m\ w\ \mathrm{ra}\cos(\alpha) - \mathrm{FT}\sin(\varphi) \end{aligned} \tag{3-A-8}$$

$$\begin{aligned} 2m\ \mathrm{Vbcx} &= [\mathrm{FT}\cos[\varphi] - m\ w\ \mathrm{rc}\sin[\alpha]) + m\ w\ \mathrm{rb} \\ 2m\ \mathrm{Vbcy} &= -m\ w\ \mathrm{rc}\cos(\alpha) + \mathrm{FT}\sin(\varphi) \end{aligned} \tag{3-A-9}$$

Here, w represents the angular velocity of the initial rotational motion, Vax and Vay the velocity of the fragment A atom after dissociation, and FT the linear momentum resulting from the repulsive force applied along to the AB bond.

Next, the following equations from the constraint of the angular momentum conservation are given for low J limit and high J limit case.

For the low J limit

$$\begin{aligned} &2m(-Vbcy \cdot xbc + Vbcx \cdot ybc) + m(Vay \cdot xc - Vax \cdot yc) + mrV_{fin} \\ &\quad = -(mwra^2 + mwrb^2 + mwrc^2) \end{aligned} \tag{3-A-10}$$

For the high J limit

$$\begin{aligned} &2m(-Vbcy \cdot xbc + Vbcx \cdot ybc) + m(Vay \cdot xc - Vax \cdot yc) + mrV_{fin} \\ &\quad = +(mwra^2 + mwrb^2 + mwrc^2) \end{aligned} \tag{3-A-11}$$

The final rotational velocity, V_{fin}, of diatomic fragment molecule can be given at the low J and high J limit case, respectively, substituting the Eq. (3-A-1)-(3-A-9) into (3-A-10) and (3-A-11).

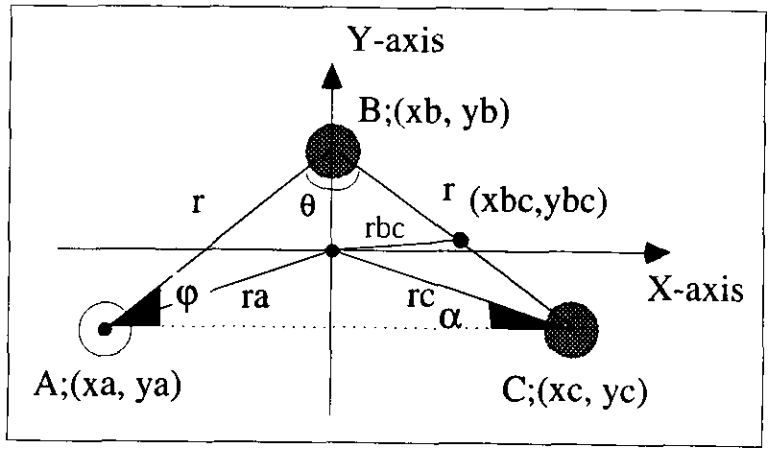

Figure III-A-1. The coordinate of tiratomic molecule for the calculation. The shaded circles represent the *N* atom and open circle represents the *O* atom. The bond lengths of *N-N* and *N-O* are fixed to be *r* and the center of mass is always located in the origin of this coordinate. The angles of θ, α, and φ are determined in the figure.

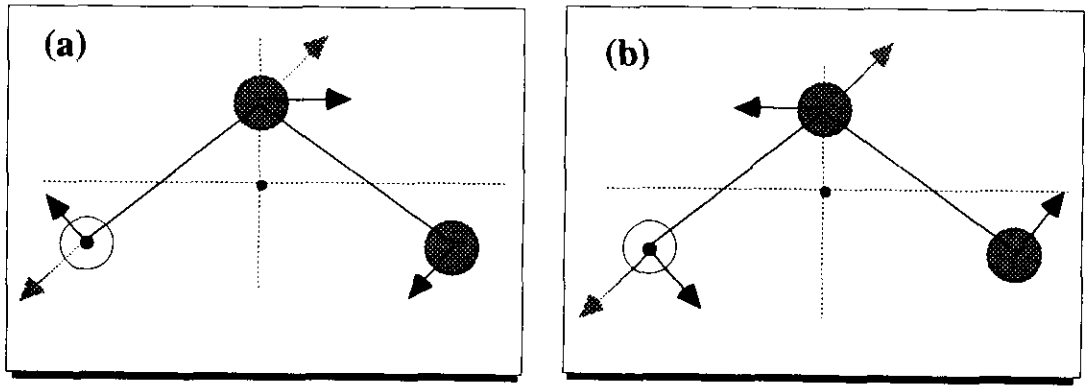

Figure III-A-2. The schematic diagram for the correlation between the direction of the momentum of initial motion (direct arrows) and the repulsive force (shaded arrows) for (a) high *J* and (b) low *J* limit. The shaded circles represent the *N* atom and open circle represents the *O* atom.

References

[1] D. M. P. Holland and J. B. West, J. Phys. B: Mol. Phys. 20 (1987) 1479;

[2] A. Haworth, D. G. Wilden and J. Comer, J. Electron Spectrosc. Relat. Phenom., 37 (1985) 291.

[3] G. Herzberg, Molecular Spectra and Molecular Structure, I. Spectra of Diatomic Molecules ; Van Nostrand: New York, 1966.

[4] A. Fujii, T. Ebata and M. Ito, J. Chem. Phys., 88 (1988) 5307; T. Ebata, A. Fujii and M. Ito, J. Phys. Chem., 91 (1987) 3125.

[5] A. Lofthus and P. H. Krupenie, J. Chem. Phys. Ref. data, 6 (1977) 113.

[6] A. D. Buckingham, B. J. Orr and J. M. Sichel., Phil. Trans. Roy. Soc. Lond. A. 268 (1970) 147.

[7] F. Merkt and T. P. Softley, Phys. Rev., 46 (1992) 302.

[8] P. Baltzer, L. Karlsson and B. Wannberg, Phys. Rev., 46 (1992) 315.

[9] M. Ogawa, and S. Ogawa, J. Mol. Spectrosc., 41 (1972) 393.

[10] H. Lefebvre-Brion and K. Yoshino, J. Mol. Spec., 158 (1993) 140.

[11] A. L. Smith, Phil. Trans. Roy. Soc. Lond. A. 268, (1970) 169.

[12] J. H. D. Eland, J. Chem. Phys., 72 (1980) 6015.

[13] D. A. Shaw, D. M. P. Holland, M. A. MacDonald, A. Hopkirk, M. A. Hayes and S. M. McSweeney, Chem. Phys. 166 (1992) 379.

[14] A. Haworth, D. G. Wilden and J. Comer, J. Electron Spectrosc. Relat. Phenom., 37 (1985) 291.

[15] P. Natalis and J. E. Collin, Int. J. Mass. Spectrum. Ion. Phys., 2 (1969) 221.

[16] G. R. Cook, P. H. Metzger and M. Ogawa, J. Chem. Phys., 58 (1968) 129; Y. Tanaka, A. S. Jursa and F. Leblanc, J. Chem. Phys., 32 (1960) 1205.

[17] J. Berkowitz and J. H. Eland, J. Chem. Phys., 67 (1977) 2740.

[18] M. Ukai, K. Kamata, S. Machida, N, Kouchi, Y. Hatano and K. Tanaka, J. Chem. Phys., 101 (1994) 5473.

[19] E. D. Poliakoff, M. H. Ho, G. E. Leroi and M. G. White, J. Chme. Phys., 85 (1986) 5529.

[20] P. M. Dehmer, J. L. Dehmer and W. A. Chupka, J. Chem. Phys., 73 (1980) 126.

[21] C. H. Dugan and D. Anthony, J. Phys. Chem., 91 (1987) 3929.

[22] N. Washida, G. Inoue, M. Suzuki and O. Kajimoto, Chem. Phys. Letters, 114 (1985) 274.

[23] C. Wittig, I. Nadler, H. Reisler, M. Noble, J. Catanzarite and G. Radharkrishnan, J. Chem. Phys., 83 (1985) 5581.

[24] C. E. Klots, J. Phys. Chem., 75 (1971) 1526.

[25] M. Quack and J. Troe, Ber. Bunsenges. Phys. Chem. 78 (1974) 240.

[26] M. Quack and J. Troe, Ber. Bunsenges. Phys. Chem. 79 (1974) 170.

[27] T. A. Spiglanin, R. A. Perry and D. W. Chandler, J. Chem. Phys., 87 (1987) 1568.

[28] G. E. Busch and K. R. Wilson, J. Chem. Phys., 56 (1972) 3626; 3638 and 3655.

[29] W. H. Fisher, T. Carrington, S. V. Filseth, C. M. Sadowski and C. H. Dugan, Chem. Phys., 82 (1983) 443.

[30] J. P. Simons and P. W. Tasker, Mol. Phys., 27 (1974) 1691.

[31] R. Schinke, Ann. Rev. Phys. Chem., 39 (1988) 39; J. Chem. Phys., 92 (1990) 2397 and references

[32] S. Mukamel and J. Jortner, J. Chem. Phys., 65 (1976) 3735.

[33] R. W. Heather and J. C. Light, J. Chem. Phys., 78 (1983) 5513.

[34] M. D. Morse, K. F. Freed and Y. B. Band, J. Chem. Phys., 70 (1979) 3604; M. D. Morse and K. F. Frees, J. Chem. Phys., 74, (1981) 4395, 78 (1983) 6045.

[35] J. Biesner, L. Schnieder, G. Ahlers, X. Xie, K. H. Welge, M. N. R. Ashfold and R. N. Dixon, J. Chem. Phys., 91 (1989) 2901.

[36] K. Weide and R. Schinke, J. Chem. Phys., 90 (1989) 7150.

[37] H. Köppel, L. S. Cederbaum and W. Domcke, Chem. Phys., 69 (1982) 175.

[38] M. Tronc, G. C. King and F. H. Read, J. Phys. B: Mol. Phys., 13 (1980) 999.

[39] H. B. Levene and J. J. Valentini, J. Chem. Phys., 87 (1987) 2594.

Chapter IV

Neutral Dissociation of OCS by Synchrotron Radiation Photoexcitation

(Chemical Physics Letters, In Preparation)

IV-1. Introduction

Neutral dissociation process competed with autoionization is characteristic decay process from molecular superexcited states in XUV region [1-5]. Two-dimensional photoelectron spectroscopy (2D-PES) using synchrotron radiation have confirmed the neutral fragmentation path from the superexcited states by observing the electron emitted by fragment autoionization [6-7]. The emission from the neutral excited fragments have revealed the specific dissociative channel following the variation of the dissociation probability as well [8-10]. However, the detailed information on the neutral dissociation have been limited, because the vibrational, rotational and electronic state distributions of the neutral fragments is difficult to be measured with one excitation source of synchrotron radiation alone. Recently the neutral dissociation from the superexcited states of *NO* have been investigated using laser two-color double resonance techniques [11], however, for the most of small molecules, the ionization potentials have been usually located at the higher photon energy than that of the case of *NO* where it is hard to access by laser excitations. Therefore, in order to investigate the neutral dissociation process over the wide energy range, the pump-probe experiments has been expected by using the synchrotron radiation as an excitation source and the laser as a probing source.

The present chapter shows the experiments for detecting the neutral species produced by undulator radiation excitation. Neutral sulfur atom, $S\ (3s^2 3p^4\ ^3P)$, produced by the undulator radiation excitation of Carbonyl Sulfide (OCS) were observed by means of the resonance enhanced multiphoton ionization (REMPI) technique. Figure 4-1 shows a schematic energy diagram of the electronic states of OCS and OCS^+ with photoexcitation, dissociation and probing pathways. One photon excitation of undulator radiation to the Rydberg states converging

to the ionization potential of $OCS^+(C^2\Sigma)$ state leads to the neutral fragments of $CO(X\,^1\Sigma)$ + $S(^3P)$. S (^3P) is ionized by two-photon excitation and one photon ionization (2+1 REMPI) process using the excimer pumped dye laser and detected by quadorapole mass filter:

$$\begin{aligned} &OCS \xrightarrow{h\nu_{SR}} CO(X^2\Sigma^+) + S(^3P) \\ &S(^3P) \xrightarrow{h\nu_{LR}} \xrightarrow{h\nu_{LR}} S^*(^3P) \xrightarrow{h\nu_{LR}} S^+(^4S_u) \end{aligned} \qquad (4\text{-}1)$$

One of the difficulty in observing fragment species is the small photon flux of the dispersed undulator radiation, and the background signal resulting from the photionization process other than (4-1). The signal count rates are calculated for the neutral fragments produced by the process (4-1).

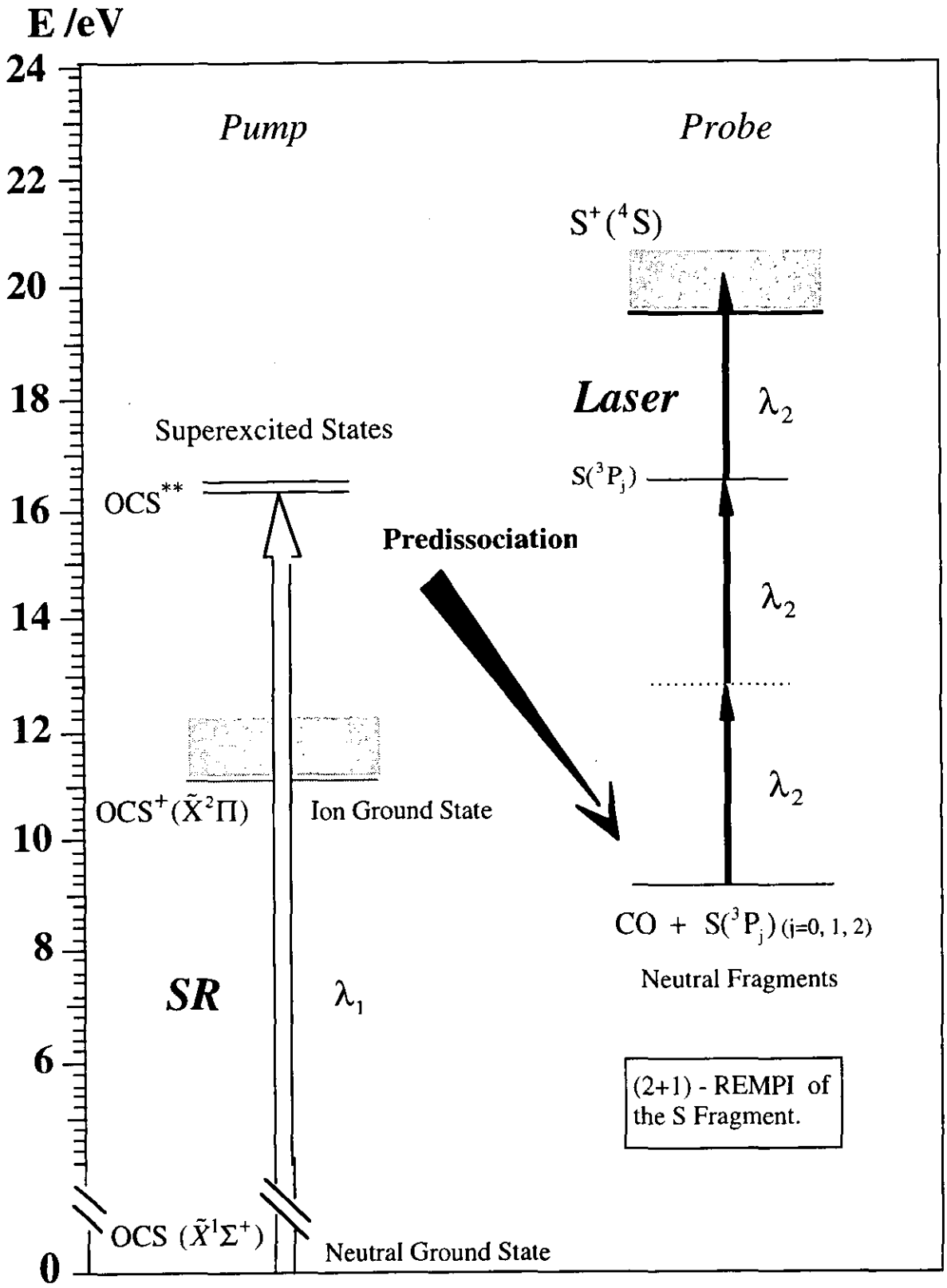

Figure 4-1. A schematic energy diagram of the electronic states of OCS and OCS^+ with photoexcitation, dissociation and probing pathway. λ_1 and λ_2 represent the photon energy of undulator radiation and laser, respectively.

IV-2. Experimental Section

Figure 4-2 shows the schematic diagram of the experimental setup. The synchrotron radiation-laser combination experiments were performed at BL3A2 (Undulator beamline) in UVSOR facility. The fundamental light of the undulator radiation dispersed by a 2.2 m grazing incidence constant deviation monochromator was used as an excitation source. The characteristics of the monochromatized undulator radiation have been described in chapter II. To achieve better signal-to-noise ratio, both the slits of the monochromator were kept at 400 μm, corresponding to an instrumental spectral resolution of 2.4 Å at the excitation energy of ~830 Å. The second harmonic of the excimer (Lambda Physik, Compex 110, XeCl) pumped dye laser (Lambda Physik, Scanmate 2, cumarine 153 dye) was used as a probing light source. The second harmonic generation was performed in a BBQ crystal (Lambda Physik, Scanmate 2 UV), yielding 0.5 - 6 mJ at ~270 nm with a line width of 0.0835 cm^{-1} [12] when the average output of eximer laser is 250 - 450 mJ $pulse^{-1}$, and the output of fundamental light is 40 - 130 mJ. Laser light was collimated by 600 mm (OL1) and 3000 mm (OL2) focal length lenses and tightly focused by a 600 mm (OL3) focal length lens placed in the front of the vacuum chamber. The radius of the laser beam was reduced to be less than 0.05 mm to ionize sulfur atom efficiently. The interrogating undulator radiation passed through the downstream of the pulsed jet (General Valve, 9 series) and molecules are photodissociated. The neutral atoms flying perpendicularly to the direction of the undulator radiation and the pulsed jet are ionized by REMPI and S^+ ions were selected by the quadorapole mass filter (Extrel, 041-12 and 7-162-8) and detected by multichannel plate (MCP). The light paths of excitation and probing source are displaced by the ion lens 2 and lens 3 (see figure 4-2). Ions and electrons produced by undulator radiation excitation alone are removed with ion lens 2 and 3 for applying the appropriate voltage to these ion lenses (see later). The removal of the photoelectron in the probing area reduces the background signal resulting from the electron impact of the neutral fragments with accelerated photoelectron. The repetition frequency of the dye laser is synchronous with one half of that for the pulsed jet, 10 - 100 Hz. The output

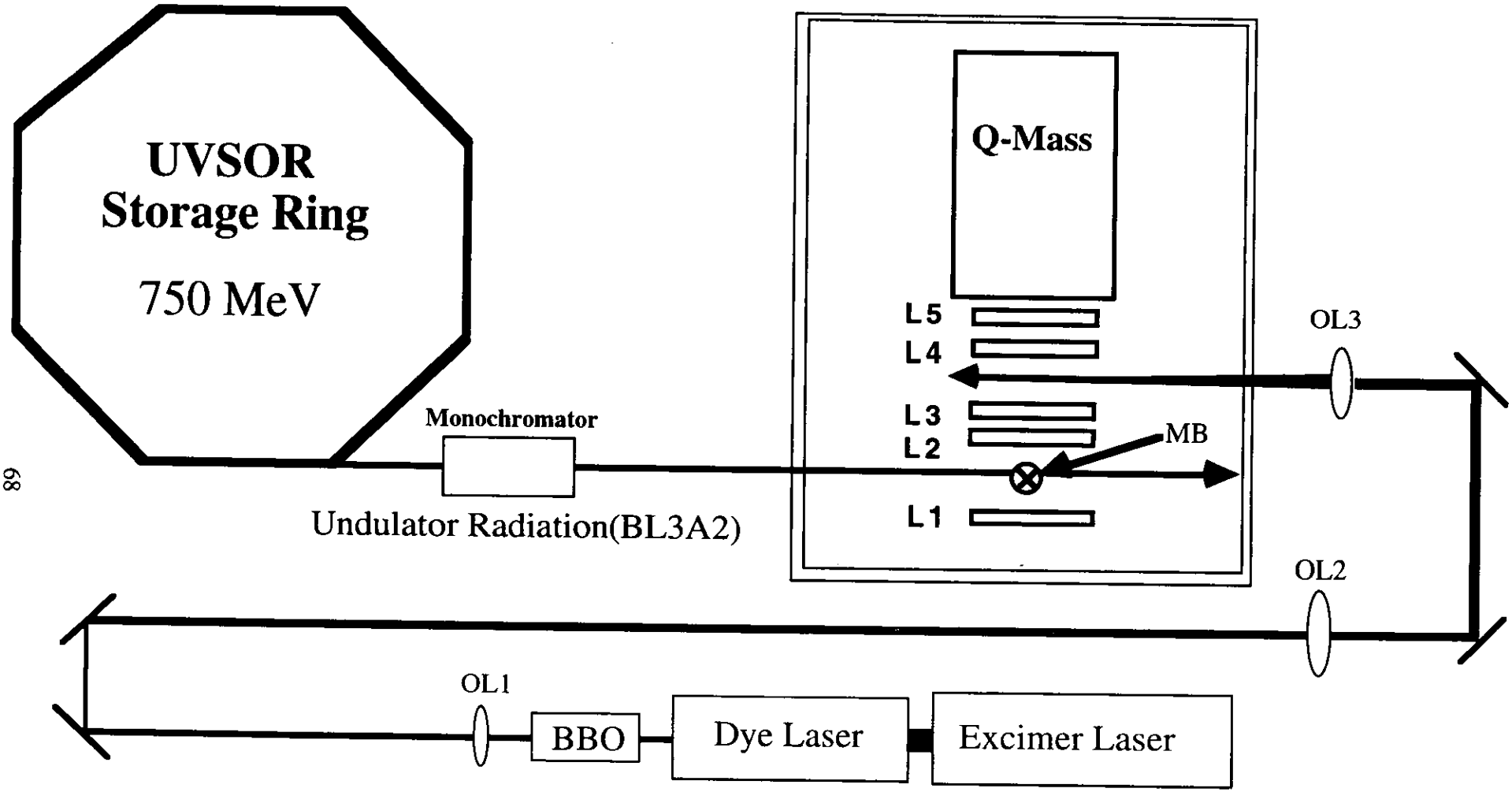

Figure 4-2. Schematic diagram for the experimental set up of REMPI spectroscopy combined with synchrotron radiation excitation. L1 - L5 represent the ion lens,es Q-Mass represents a quadorapole mass filter. The pathway of undulator radiation and laser is displaced on 5 cm in distance (see text). MB represents a pulsed jet. Three optical lenses (OL1 - OL3) are used to focus the lase beam.

of MCP is gated on the time when the pulsed jet opens with some delay in order to suppress the background noise. The number of ions are counted separately for laser on (Channel A) and laser off (Channel B) periods by a two-channel gated photon counter (EG&G, 994). Ion counts resulting from the undulator radiation excitation alone is removed by subtracting the number of ions in channel A from those in channel B (= A - B). The same measurement is repeated with the undulator radiation being shuttered, giving the signal counts A' and B', respectively, and the value A' - B' yields the number of ions due to multiphoton ionization with a laser alone. The number of the ions depending on both of the undulator radiation and laser is thus obtained by the expression (A - B) - (A' - B').

The crucial factor is to remove the background signal resulting from the ionization process, for present case, S^+ produced by the processes other than (4-1). The following four dissociation and ionization processes are considered as those leading to the background signals. One of these are coming from synchrotron radiation excitation alone, and next two of them are coming from a laser excitation alone. One is resulting from both laser and synchrotron radiation excitation of OCS. The undulator radiation excitation directly produces S^+ above the lowest dissociative ionization process (D = 13.52 eV) [13]:

$$OCS \xrightarrow{h\nu_{SR}} CO(X^1\Sigma^+) + S^+(^4S_u) \qquad (4\text{-}2)$$

The threshold of the dissociative ionization process is summarized at Table 4-1 as well as the ionization energy of OCS. To remove the S^+ ion resulting from this process, the light pass of both excitation and probe source is separated and the electronic fields are applied to the direction so as to get the ions to fly to the opposite direction to the quardrapole mass filter.

One photon excitation of OCS^+ produced by three-photon ionization of OCS by a laser excitation alone also leads to the products of $CO(X\ ^2\Sigma^+) + S^+(^4S_u)$:

$$OCS \xrightarrow{3h\nu_{LR}} OCS^+(X^2\Pi) \xrightarrow{h\nu_{LR}} CO(X^1\Sigma^+) + S^+(^4S_u). \quad (4\text{-}3)$$

Furthermore, the 2+1 multiphoton ionization process of $S(^3P)$ produced by two photon resonant

photodissociation of OCS can be observed with the excitation of the probe laser alone, which gives a total of five photon process of OCS. In this process two-photon excitation energy to the dissociative excited state of OCS accidentally accords with that of the resonant photon energy corresponding to the transition of S($5p$, ^3P) ← S($3p^4$, ^3P).

$$\begin{aligned} &OCS \xrightarrow{2h\nu_{LR}} CO(X^1\Sigma^+) + S(^3P) \\ &S(^3P) \xrightarrow{h\nu_{LR}} \xrightarrow{h\nu_{LR}} S^*(^3P) \xrightarrow{h\nu_{LR}} S^+(^4S_u) \end{aligned} \qquad (4\text{-}4)$$

To remove the S^+ ions resulting from these mutiphoton processes, the efficiency of the multiphoton process should be reduced by decreasing the peak power of lasers, which can be attained by defocusing the laser beam on the ionization area.

Finally, the dissociative ionization process for producing S atom as a counterpart of fragment ions by undulator radiation excitation alone competes with the neutral dissociation process (4-1):

$$\begin{aligned} &OCS \xrightarrow{h\nu_{SR}} CO^+(X^2\Sigma^+) + S(^3P) \\ &S(^3P) \xrightarrow{h\nu_{LR}} \xrightarrow{h\nu_{LR}} S^*(^3P) \xrightarrow{h\nu_{LR}} S^+(^4S_u) \end{aligned} \qquad (4\text{-}5)$$

The sulfur atom produced by the process (4-1) is difficult to be distinguished with that formed by the process (4-5). Thus the experiments were performed where the excitation energy of undulator radiation is smaller than that of the dissociation limit for process (4-5), namely, 17.17 eV.

Table 4-1. Adiabatic ionization potentials and Dissociation limit of OCS [6].

Key[#1]	Energy / eV[#2]	Species	Symmetry
D	3.16	$CO(A^1\Pi) + S(^3P)$	$^3\Sigma^-, ^3\Pi$
D	9.14	$CO(a^3\Pi) + S(^3P)$	$^{1,3,5}\Delta, ^{1,3,5}\Pi, ^{1,3,5}\Sigma^+, ^{1,3,5}\Sigma^-$
D	10.03	$CO(a'^3\Pi) + S(^3P)$	$^{1,3,5}\Pi, ^{1,3,5}\Sigma^-$
D	10.91	$CO(d^3\Pi) + S(^3P)$	$^{1,3,5}\Delta, ^{1,3,5}\Pi, ^{1,3,5}\Sigma^+, ^{1,3,5}\Sigma^-$
D	11.17	$CO(A^1\Pi) + S(^3P)$	$^3\Delta, ^3\Pi, ^3\Sigma^+, ^3\Sigma^-$
I_P	11.174	$OCS^+(X^2\Pi\ [0,0,0])$	
D	13.49	$CO(b^3\Pi) + S(^3P)$	$^{1,3,5}\Pi, ^{1,3,5}\Sigma^-$
D	13.88	$CO(B^1\Sigma^+) + S(^3P)$	$^3\Sigma^-, ^3\Pi$
D	14.38	$CO(e^3\Sigma^+) + S(^3P)$	$^{1,3,5}\Pi, ^{1,3,5}\Sigma^-$
D	14.41	$CO(C^1\Sigma^+) + S(^3P)$	$^3\Sigma^-, ^3\Pi$
D	14.62	$CO(E^1\Sigma^+) + S(^3P)$	$^3\Sigma^-, ^3\Pi$
D	14.65	$CO(c^3\Sigma^+) + S(^3P)$	$^{1,3,5}\Pi, ^{1,3,5}\Sigma^-$
I_P	15.075	$OCS^+(A^2\Pi\ [0,0,0])$	
D	15.48	$CO(F^1\Pi) + S(^3P)$	$^3\Delta, ^3\Pi, ^3\Sigma^+, ^3\Sigma^-$
I_P	16.041	$OCS^+(B^2\Sigma^+\ [0,0,0])$	
D	16.22	$CO(G^1\Sigma^+) + S(^3P)$	$^3\Delta, ^3\Pi, ^3\Sigma^+, ^3\Sigma$
I_P	17.958	$OCS^+(C^2\Sigma^+\ [0,0,0])$	

[#1] The symbols I_p and D refer to the adiabatic ionization potential and the limit for dissociation.

[#2] All energies are measured with respect to the neutral ground state $OCS\left[X^1\Pi(0,0,0)\right]$.

[#3] This is the energy at most intense peak observed in photoelectron spectrum.

IV-3. Results and Discussion

Figure 4-3 shows a REMPI spectrum of S($3s^23p^4$, $^3P_2$) as a function of the probe laser wavelength in the region involving of the two-photon transitions, S($3s^23p^35p$, ^3P_J) ←S($3s^23p^4$, $^3P_2$). The excitaion photon energy of the undulator radiation was fixed at 16.5 eV. The maximum at 269.290 nm is considered to comprise the two peaks resulting from transitions from S($3s^23p^4$, $^3P_2$) to S ($3s^23p^35p$, $^3P_1$) and S($3s^23p^35p$, $^3P_2$) though they are not separated due to low signal-to-background ratio [14]. In the shorter wavelength, the peak resulting from the transition S($3s^23p^4$, $^3P_2$) to S ($3s^23p^35p$, $^3P_0$) should be observed, but in this spectrum that peak is embedded in the noise level. In addition to S ($3s^23p^4$, $^3P_2$), a REMPI signal of S ($3s^23p^4$, $^3P_0$) at 271.375 nm was detected, which corresponds to a transition from S ($3s^23p^4$, $^3P_0$) to S ($3s^23p^35p$, $^3P_0$). The laser power dependence of the peak intensity confirms that these REMPI process are three photon process.

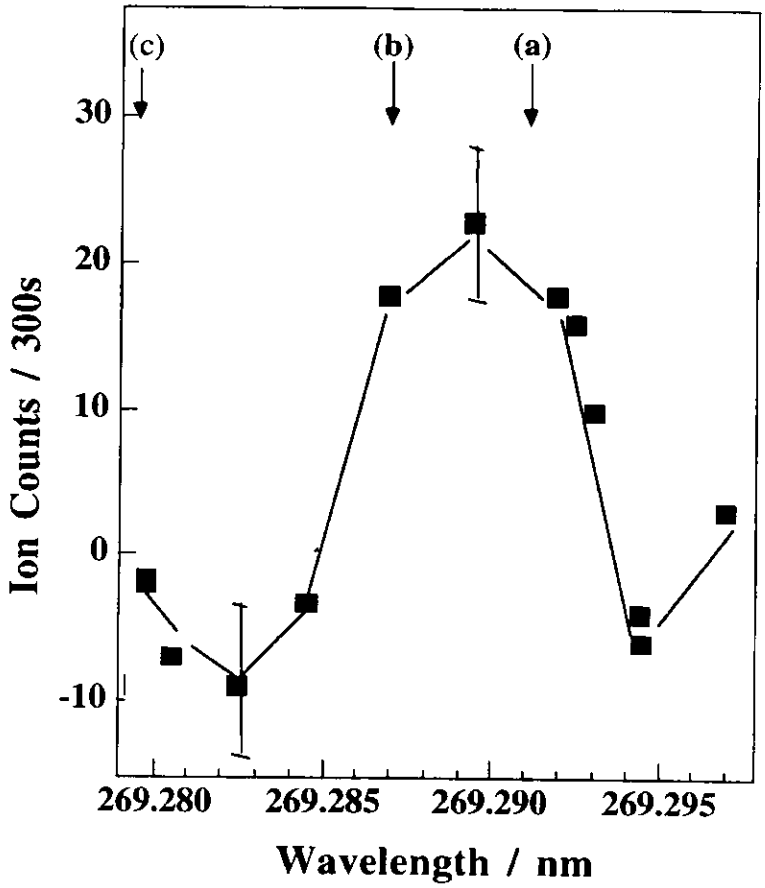

Figure 4-3 The REMPI spectrum of S ($3s^23p^4$, $^3P_2$) produced by undulator radiation excitation of OCS at 16.5 eV. The arrows of (a), (b), and (c) represents the peaks resulting from two photon transitions (a) S ($3s^23p^35p$, $^3P_2$) ← S($3s^23p^4$, $^3P_2$), (b) S($3s^23p^4$, $^3P_1$) ← S($3s^23p^35p$, $^3P_2$), and (c) S ($3s^23p^35p$, $^3P_0$) ← S($3s^23p^4$, $^3P_2$).

The signal count rate of the S^+ ion produced from the 2+1 REMPI process followed by the photodissociation of OCS can be estimated. The number of molecules in the Rydberg states, n_{SR} [molecules pulse^{-1}], produced by one pulse of undulator radiation excitation is given by

$$n_{SR} = \sigma_{SR} I_{SR} n_0 \qquad (4\text{-}6)$$

where σ_{SR} [cm^2] represents the absorption cross section for the given Rydberg state of OCS, I_{SR} [photons cm^{-2} pulse^{-1}] represents the photon density of the one pulse of undulator radiation in the unit area and n_0 [molecules cm^{-3}] is the number of molecules in unit volume estimated by the state equation for ideal gases. The number of S^+ ions in unit volume, n_{SR} produced by a 2+1 REMPI spectroscopy is given by

$$n_{LR} = C_{LR} n_{SR} f_1 f_2 f_3 f_4 \qquad (4\text{-}7)$$

where C_{LR} represents the ionization efficiency for two-photon resonant one-photon ionization process, f_1, f_2, f_3 and f_4 represent the some factors as defined later. At the small photon flux of laser, the value of C_{LR} is approximately given by [15]

$$C_{SR} = \sigma^{I}_{LR} \sigma^{II}_{LR} (I_{LR})^3 (\Delta t)^2 \qquad (4\text{-}8)$$

where Δt represents the temporal pulse width (full width half maximum) of a probe laser, I_{SR} [photons s^{-1} cm^{-2}] represents the number of photons in one pulse and in unit area of a probe laser, and σ^{I}_{SR} [cm^2] and σ^{II}_{SR} [cm^2] represent the one photon non-resonant ionization and two photon resonant absorption cross sections, respectively [15]. At the large value of I_{SR}, the Eq. (4-8) is ruled out and the value of C_{SR} is close to unity [15]. The value of f_1 is given by

$$f_1 = F_{SR} \times \tau_f \qquad (4\text{-}9)$$

where τ_f represents the time when the fragments go through the excitation volume, which is

calculated by the fragment velocity and the beam radius of a probe laser[#1]. The value of F_{SR} represents the repetition frequency of the undulator radiation, f_2 represents the ratio of the partial cross section of the electronically ground state of $S(^3P_J)$ to the absorption cross section of Rydberg states, and f_3 represents the ratio of the spectral band width of the probe laser to that of the inhomogeneous broadened band width of a single rotational level resulting from the doppler effect. In the present case, the value of f_3 is taken to be unity since the doppler width is smaller than the spectral resolution of the laser. f_4 represents that the dilution factor resulting from the distance of the paths between the probe laser and excitation undulator radiation, which is estimated by the angular dependence of fragmentation and the ionization volume of a probe laser. Finally, the signal count rate, cps[s^{-1}], of S^+ is given by

$$cps[s^{-1}] = n_{LR}\gamma_1\gamma_2 F_{LR} \qquad (4\text{-}10)$$

where γ_1 represents the efficiencies determined by the geometry of the ion lens and applied electric field, γ_2 represents the quantum efficiency of the MCP, V is the excitation volume for undulator radiation, and F_{LR} is the repetition frequency of the probe laser.

Figure 4-4 shows the estimated signal count rate of S^+ as a function of the photon flux of the undulator radiation. The values of parameters are taken as follows : I_{SR} = 8 × 10^{12} [photons s^{-1} mm^{-2}], σ_{SR} = 10 × 10^{-18} [cm^2], n_0 = 3 × 10^{11} [molecules cm^{-3}] corresponds to the ambient pressure of 1 × 10^{-5} torr. Other parameters of f_2, f_4, γ_1 and γ_2, are assumed to be unity, since they are difficult to be estimated. The counts rate is calculated to be 13 [cps] at the photon flux of the dispersed undulator radiation of BL3A2 to be the 8 × 10^{12} photons s^{-1} mm^{-2}. The difference between obserbed and calculated one is resulting from that the parameters that have taken to be unity for tentatively must be less than unity actually.

[#1] If the lifetime of the electronic states of fragments is smaller than the value of τ_p, τ_f in Eq. 4-9 is replaced by the lifetime. In the prsent case, the lifetime of $S(^3P)$ is much larger than the value of τ.

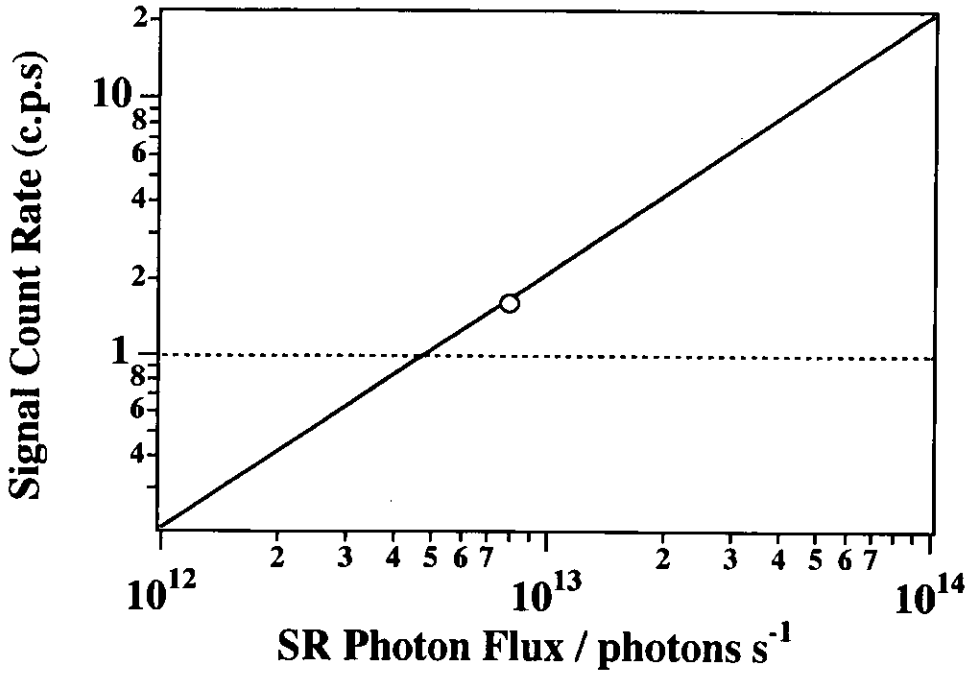

Figure 4-4. Signal count rate of S^+ as a function of the photon flux of the undulator radiation. Open circle represents the calculated signal count rate corresponding to the photon flux of undulator radiation (= 8×10^{12} photons s^{-1})

Conclusion

This chapter shows the REMPI spectrum of S(^{3}P) produced by the undulator radiation excitation of OCS at 16.65 eV. The signal count rate is calculated for the present pump-probe spectroscopy. For our best knowledge, the present study is the first report that the neutral species produced by undulator radiation excitation can be detected by REMPI spectroscopy.

References

[1] G. R. Cook and M. Ogawa, J. Chem. Phys., 51 (1969) 647.

[2] F. Carnovale, A. P. Hitchcock, J. P. D. Cook and C. E. Brion, Chem. Phys., 66 (1982) 249.

[3] M. G. White, K. T. Leung and C. E. Brion, J. Elec. Spectrosc. Relat. Phenom., 23 (1981) 127.

[4] D. A. Shaw, D. M. P. holland, M. A. MacDonald, A. Hopkirk, M. A. Hayes and S. M. McSweeney, Chem. Phys., 163 (1992) 387.

[5] I. Nenner, M. J. Hubin-Franskin, J. Delwiche, P. Morin, and S. Bodeur, J. Mol. Struct., 173 (1988) 269.

[6] A. Tabché-Fouhalie, M. J. Hubin-Franskin, J. P. Delwiche, H. Fröhlich, K. Ito, P. M. guyon and I. Nenner, J. Chem. Phys., 79 (1983) 5894.

[7] Y. Hikosaka, H. Hattori, T. Hikida and K. Mitsuke, J. Chem. Phys., 107 (1997) 2950.

[8] Y. Hikosaka, H. Hattori, K. Mituke, J. Chem. Phys., 110 (1999) 335.

[9] S. Machida, M. Ukai, M. Kitajima, K. Kameta, N. Kouchi, Y. Hatano, T. Hayashi and K. Ito, J. Elec. Spectrsc. Relat. Phenonm. 80 (1996) 25.

[10] S. Machida, M. Ukai, M. Kitajima, K. Kameta, N. Kouchi, Y. Hatano, T. Hayashi and K Ito, J. Phys. Chem., 101 (1997) 656.

[11] A. Fujii, N. Morita, Chem. Phys. Letters, 182 (1991) 304; J. Chem. Phys., 98 (1993) 4581.

[12] *Instrumental Manuall* of the excimer pumped dye laser, *Lambda Physik.*

[13] Y. Hikosaka, H. Hattori, T. Hikida and K. Mitsuke, J. Chem. Phys., 107 (1997) 2950.

[14] P. Brewer, N. Van Veen, and R. Bersohn, Chem. Phys. Letters, 91 (1982) 126.

[15] P. Cremaschi, P. M. Johnson and J. L. Whitten, J. Chem. Phys., 69 (1978) 4341.

Chapter V General Conclusion

This study shows the development of experimentals for using the synchrotron radiation and laser combination techniques for investigating the gaseous molecular ionization and dissociation dynamics in XUV. In our best knowledge, this is the first report that the ions and neutral fragments formed by undulator radiation excitation are directly detected by means of the LIF and REMPI spectroscopy. The experimental results achieved in this study are summarized in brief. The rotational structures of the electronic transition $N_2^+(B\ ^2\Sigma_u^+,\ v' = 0) \leftarrow N_2^+(X\ ^2\Sigma_g^+,\ v'' = 0)$ were observed with the spectral resolution of 1.6 cm^{-1}, which is much higher than a conventional photoelectron analyzer. The rotational state distributions of $N_2^+(X\ ^2\Sigma_g^+,\ v'' = 0)$ formed by undulator radiation excitation of N_2O were also observed. The neutral $S(^3P_J)$ fragment produced by the undulator radiation excitation of OCS at 16.56 eV were detected by a REMPI spectroscopy.

The aim for investigating the dynamics of superexcited state by measuring the internal state distribution of photoproducts are not fully achieved in this study, probably because of the low signal-to-noise ratios of both SR-LIF and SR-REMPI spectroscopy. However, the important thing is to indicate whether the synchrotron radiation-laser combination experiments are possible or not for studying the molecular dynamics in XUV. These kind of combination experiments, *i.e.*, probing the photoproducts by a laser spectroscopy followed by the synchrotron radiation photoexcitation, should be performed in any synchrotron radiation facilities in order to extend the possibility of the synchrotron radiation as an excitation source in XUV region.

The signal count rates observed in this study are very week, ~ 2 cps for $N_2^+(X^2\Sigma_g^+,\ v = 0)$ from N_2 by a *SR-LIF* spectroscopy, and ~ 0.6 cps for the $S(^3P_J)$ from OCS by a *SR-REMPI* spectroscopy. The fragment ions of $N_2^+(X\ ^2\Sigma_g^+,\ v = 0)$ dissociating from N_2O are able to detect by increasing the ion signal counts using an ion trap. However, an ion trap has a difficulty for measuring a nascent measurement of the rotational state distribution, because the collision effect in the trap must be considered. The reason for using ion trap purposely in

spite of the difficulty is to make a confirm what number of signal counts are needed for probing the fragment ions. So it is clear now, what kind of improvement is required for getting the signal count rate enough to investigate fully the molecular superexcited state dynamics in XUV.

For detecting the fragment ions instead of using an ion trap, at least 10^2 - 10^3 times signal counts are required for a SR-LIF spectroscopy. This can be attained by increasing the detection efficiency of fluorescence. For instance, using semi-parabolic mirror is promising for getting more than 10^3 times increase of the signal counts rate compared with that of present system. Constructing an optical multipass cavity at the excitation area would be also available to get the signal counts increasing more than 20 times.

As for SR-REMPI spectroscopy, the signal counts at least more than 10^2 - 10^3 times is required for measuring the yield curves and the internal state distributions of any fragments. When detecting the fragment molecules, the observed signal counts are inferred to be lower than those for fragment atoms becasue of the internal state distribution of fragments molecules.

The cavity-ringdown techniques [1] would be useful for getting more REMPI signal counts. The laser light into the optical cavity composed by two spherical mirrors can be reflected many times, depending on the reflexivity of the cavity mirrors. For instance, the mirrors with the reflexivity of 99.99 % can achieve about 1000 times of reflection during the ringdown time [1]. The disadvantage of this technique for applying the SR-REMPI spectroscopy is in that the laser intensity decreases when it goes into the mirror at incident angle. However, it can be got over when a large with laser intensity enough to achieving the efficient REMPI process is employed. For instance, if the ionization efficiency for the 2+1 REMPI process is unity at the power of 10 μJ /pulses, that of 10 mJ /pulse is necessary with 99.99% mirror. Such a large peak intensities can be easily obtained by using a conventional excimer pumped dye laser.

The synchrotron radiation and laser combination experiments can be also applied another type of experiments, like the double-resonance spectroscopy. In the inner valence region, the multiple excitation process characterizes their complicated absorption and following

decay features. If we excite the electrons one by one using synchrotron radiation and laser, it is expected to prepare the excited state with a selected electronic configurations, in particular, that can not be accessed from electronically ground states with one photon excitation. This may result in finding the new dissociation or ionization path leading to the site selective dissociation, and controlling the dissociation and ionization processes.

Recently, the higher-harmonic generation techniques using lasers with high pulse intensity has been developing as an excitation source in XUV with a ultrashort pulse [2-3]. Not only pulse energy but also brilliance are comparable with those of the third generation synchrotron radiation emitted from bending magnet below ~ 200 eV [4]. On the other hands, free electron laser using linac has been also developing as an coherent X ray source [5]. In next generation, the combination experiments using these two types of light source will come to the center stage for the study of dynamics in XUV.

References

[1] A. O'Keefe and D. A. G. Deacon, Rev. Sci. Instrum., 59 (1988) 2544.
[2] A. Rundquist, C.G. Dufee III, Z. Chang, C. Herne, M. M. Murnane, and H. C. Kapteyn, Science, 280 (1998) 1412,
[3] P. Corkum, Nature, 403 (2000) 845.
[4] S. Watanabe, *"Ultrashort Pulse Generation and Frequency Conversion"*, Kikan Kagaku Sousetsu, 44 (2000) 11.
[5] DESSY, in Germany.

Publications

1. H. Niikura, M. Mizutani and K. Mitsuke. *"Rotational State Distribution of N_2^+ Produced from N_2 or N_2O Observed by a Laser-Synchrotron Radiation Combination Technique"*
Chemical Physics Letters, Vol. 315 (2000) pp.45 - 52.

2. M. Mizutani, H. Niikura, A. Hiraya and K. Mitsuke. *"Laser-Induced Fluorescence Excitation Spectroscopy of N_2^+ produced by VUV photoionization of N_2 and N_2O".*
Journal of Synchrotron Radiation, Vol. 5 (1998) pp. 1067 - 1071.

Other Publications

1. H. Niikura and S. Hirayama. *"Shift from an Inverse to a Normal Isotope Effect on the Non-radiative Decay rate of Anthracene-d_{10} observed under Partially Jet-cooled Conditions".*
Chemical Physics Letters, Vol.296 (1998) pp. 343 - 349.

2. H. Niikura, U. Graf and S. Hirayama. *"Intramolecular Non-radiative Relaxation from the First Excited Singlet Background Manifolds of Anthracene and 9,10-dichloroanthracene in Partially Jet - Cooled States".*
Chemical Physics Letters, Vol. 266 (1997) pp. 217 - 222.

3. U. Graf, H. Niikura and S. Hirayama. *"Fluorescence Quenching by Oxygen. Lack of Evidence for the Complex Formation of Oxygen with 9-Cyanoanthracene and Anthracene in a Supersonic Free Jet".*
Journal of Physical Chemistry, Vol 101, (1997) pp. 1292 - 1298.

4. M. Maeda, U. Graf, H. Niikura, M. Okamoto and S. Hirayama. *"Thermal Energy Assisted Heavy Atom Effect: Fluorescence Quenching of 9-Cyanoanthacene in the Supercritical Fluid of Xe".*
Chemical Physics Letters, Vol. 257 (1996) pp. 175 - 180.

5. U. Graf, H. Niikura and S. Hirayama. *"Laser Free Measurement of Absorption and Fluorescence Excitation Spectra in a Supersonic Free Jet".*
Review of Scientific Instruments, Vol. 67 (1996) pp. 406 - 409.